Digital Discovery

ROYAL SOCIETY OF CHEMISTRY

PAPER

View Article Online
View Journal | View Issue

Check for updates

Cite this: *Digital Discovery*, 2023, **2**, 422

# An open-source environmental chamber for materials-stability testing using an optical proxy†

Rodolfo Keesey, ‡*[a] Armi Tiihonen, ‡*[bc] Alexander E. Siemenn, [c] Thomas W. Colburn, [d] Shijing Sun,[c] Noor Titan Putri Hartono, [c] James Serdy,[c] Margaret Zeile, [a] Keqing He,[a] Cole A. Gurtner,[d] Austin C. Flick,[d] Clio Batali,[c] Alex Encinas,[c] Richa R. Naik,[c] Zhe Liu,[c] Felipe Oviedo,[c] I. Marius Peters,[c] Janak Thapa,[c] Siyu Isaac Parker Tian,[e] Reinhold H. Dauskardt,[d] Alexander J. Norquist *[a] and Tonio Buonassisi *[c]

This study is motivated by the desire to produce a low-cost, high-precision, high-throughput environmental chamber to test materials and devices under elevated humidity, temperature, and light. This paper documents the creation of an open-source tool with a bill of materials as low as US$2,000, and the subsequent evolution of three second-generation tools installed at three different universities spanning thin films, bulk crystals, and thin-film solar-cell devices. We introduce an optical proxy measurement to detect real-time phase changes in materials. We present correlations between this optical proxy and standard X-ray diffraction measurements, describe some edge cases where the proxy measurement fails, and report key learnings from the technology-translation process. By sharing lessons learned, we hope that future open-hardware development and translation efforts can proceed with reduced friction. Throughout the paper, we provide examples of scientific impact, wherein participating laboratories used their environmental chambers to study and improve the stabilities of halide-perovskite materials. All generations of hardware bills of materials, assembly instructions, and operating codes are available in open-source repositories.

Received 23rd August 2022
Accepted 30th January 2023

DOI: 10.1039/d2dd00089j

rsc.li/digitaldiscovery

Open Access Article. Published on 13 February 2023. Downloaded on 1/29/2026 5:10:34 AM.
This article is licensed under a Creative Commons Attribution-NonCommercial 3.0 Unported Licence.

## 1. Introduction

Quantifying and predicting long-term stability in realistic operating environments is of interest to a broad range of materials, from energy devices to marine and offshore environments.[1–5] However, accelerated environmental testing today is often time-intensive and expensive, limiting the speed of materials innovation. Commercial stability chambers can cost tens of thousands of US dollars, with fully integrated solar device stability testing systems can cost up to US$60 000, and may require additional modification to generate consistent-quality degradation data for a specific application.[6] Given the rise of automated experimentation systems and artificial intelligence in materials discovery,[7–9] developing stability testing equipment that can both mitigate the cost of longitudinal testing and provide high quality, machine-interpretable degradation data has grown in importance, addressing a bottleneck in high-throughput materials discovery.

To meet this need, we introduce a low-cost, open-source environmental chamber. Our chambers range from US$2 000–$7 500 depending on configuration, and offer environmental control as well as *in situ* monitoring. Although the design principles of the chamber are broadly applicable, we designed the chamber specifically to test halide perovskites, a class of functional materials with nascent applications in photovoltaic absorbers, light-emitting devices, and X-ray detectors, among others.[10,11] Commercialization of the aforementioned devices is often limited by poor environmental stability under operating conditions.[12–16] This has led to diverse efforts to modify perovskite alloy composition and device architecture,[17] with the aim of improving environmental stability and widening accessibility by reducing price. The extent and mechanism by which newly synthesized alloys and devices degrade under environmental conditions is a subject for study.[18–20]

[a]*Haverford College, 370 Lancaster Avenue, Haverford, 19041, Pennsylvania, USA. E-mail: rkeesey@fordham.edu ; anorquis@haverford.edu*

[b]*Department of Applied Physics, Aalto University, P.O. Box 11100, Aalto, FI-00076, Finland. E-mail: armi.tiihonen@gmail.com*

[c]*Massachusetts Institute of Technology, Cambridge, MA 02139, USA. E-mail: buonassisi@mit.edu*

[d]*Department of Materials Science and Engineering, Stanford University, Stanford, CA 94305, USA*

[e]*Low Energy Electronic Systems (LEES), Singapore-MIT Alliance for Research and Technology (SMART), Singapore 138602, Singapore*

† Electronic supplementary information (ESI) available. See DOI: https://doi.org/10.1039/d2dd00089j

‡ Contributed equally.



© 2023 The Author(s). Published by the Royal Society of Chemistry

Open Access Article. Published on 13 February 2023. Downloaded on 1/29/2026 5:10:34 AM.
This article is licensed under a Creative Commons Attribution-NonCommercial 3.0 Unported Licence.

We designed this open-source hardware platform to be easily reconfigurable to a range of materials and form factors. To test this flexibility in the principles of construction and operation for the environmental chamber, we report the original hardware design suitable for testing bare thin films, and also three subsequent equipment modifications, including adaptations to study either perovskite devices or bulk crystals. Two of these modifications occurred in different laboratories. We report key learnings from this technology translation process with the goal of defining a set of best practices for open hardware reporting. We observe that open hardware is common for foundational chemical tasks (*i.e.*, liquid handling[21–25]) but has been slower to realize for more specialized tasks like stability testing. Ideally, sharing these learnings may expedite the processes of creating and adapting future specialized open hardware.

Another key element to high-throughput testing is the development and validation of proxy measurement techniques. We posit that the many physically- and chemically-meaningful signals have optical signatures that are often overlooked. Here, we use a visible-light camera as a proxy for perovskite phase transitions, validate this proxy using X-ray diffraction (XRD), and describe the limits under which this proxy measurement is valid. Using an optical proxy for stability accelerates the rate of data acquisition by more than an order of magnitude and enables low-cost *in situ* measurements during environmental degradation.

In summary, we report an open-source aging chamber design, designed for high-throughput, semi-automated stability measurements of perovskite samples. This article is structured as follows: first, we establish the design principles of the environmental chamber and present evidence for perovskite color change being a suitable proxy for perovskite degradation, and determine the limits of proxy validity. Second, we describe the chamber versions. Third, we discuss our process of open-hardware dissemination between three different laboratories, and identify principles that may facilitate similar efforts in the future. By firstly sharing all the designs and secondly discussing the development process itself, we hope to encourage wider adoption of specialized open-hardware efforts in materials research, and facilitate further evolution of this environmental chamber design in new applications and laboratories.

## 2. Conception

### 2a. Generating machine-compatible stability data

An open-hardware design for an environmental chamber was originally conceived at MIT to leverage community inputs and refinements in subsequent generations. The build guide was shared with collaborators, and the hardware design evolved into a second generation in parallel efforts at three different sites (Fig. 1): Haverford (Norquist laboratory), Stanford (Dauskardt laboratory), and the original MIT group (Buonassisi laboratory).

Our hardware-design goal was to generate machine compatible degradation data to aid halide-perovskite stability research. We wanted the degradation chamber to fulfill four intertwined requirements to reach machine compatibility: (1) the ideal device should be capable of producing degradation data with sufficiently high throughput for the machine learning algorithms. Linked to this requirement, (2) the device should be low cost to enable expansion when necessary. Experimental variance can lead to erroneous conclusions, especially in high-throughput experimental workflows guided by machine learning (garbage in, garbage out). Thus, the data should have (3) low variations and (4) preferably no physical contacts to the samples.

These criteria require judicious selection of the response variable for the *in situ* degradation system. Direct observations of phase transformations *via* XRD normally require removing samples from the aging chamber, perturbing the aging process. *In situ* electrical measurements provide useful information, but require electric contacts that can be prone to (intermittent) faults. Thus, we opted for a non-invasive optical signature as a proxy for sample degradation.

Because spectroscopy is a widely accepted method in kinetics experimentation, we propose that optical changes in the visible light spectra can be a viable substitute when samples must be observed noninvasively *in situ,* especially for materials like lead halide perovskites which have degradation pathways in the visible spectrum. Color change is often used in chemical experimentation as an indication of reactivity. In food science, automated color change analysis has been instrumental in quality assessment and sorting.[26–28] General chemistry pedagogical experimentation with kinetics in acid and base reactions leans heavily upon color change indicators,[29] and more machine-driven versions using smartphone cameras have since automated the analysis of optical changes to determine rate law parameters.[30]

Color extends beyond a qualitative measure and can also be compared between laboratories when it is properly calibrated to account for the effects of illumination conditions and camera devices.[31] Methods such as 3-dimensional thin plate spline or root-polynomial regression are applied to convert the colors seen by the camera to the colors they would look like under a standardized reference illuminant using a reference color chart as a basis for the transformation.[32,33] Calibrated color has been previously introduced as a quantitative metric to evaluate dye solar cell degradation[34,35] and especially in color analysis applications that involve multiple devices or sites. Furthermore, calibrated color is useful when small-area colorimeters are not sufficient due to the spatial variability of the samples, such as in the food industry[26,28,36] or textiles integrated with photovoltaics.[62] Recently, *in situ* colorimetric analyses have been reported for a wide variety of non-invasive studies, for reaction kinetics in catalyst degradation of palladium(II) systems,[37] and as an alternative method of evaluation for real time catalytic hydrogen evolution.[38,39]

We hypothesize that materials properties of interest such as electronic structure, composition, and defects have optical signatures, which can be rapidly measured and correlated with high-fidelity structural or electronic characterization methods. This is not a bidirectional relationship; while the presence of color change indicates some mechanism of material decomposition, the lack of color change does not imply stability. An optical proxy is thus a strong but noncomprehensive indication

Open Access Article. Published on 13 February 2023. Downloaded on 1/29/2026 5:10:34 AM.
This article is licensed under a Creative Commons Attribution-NonCommercial 3.0 Unported Licence.

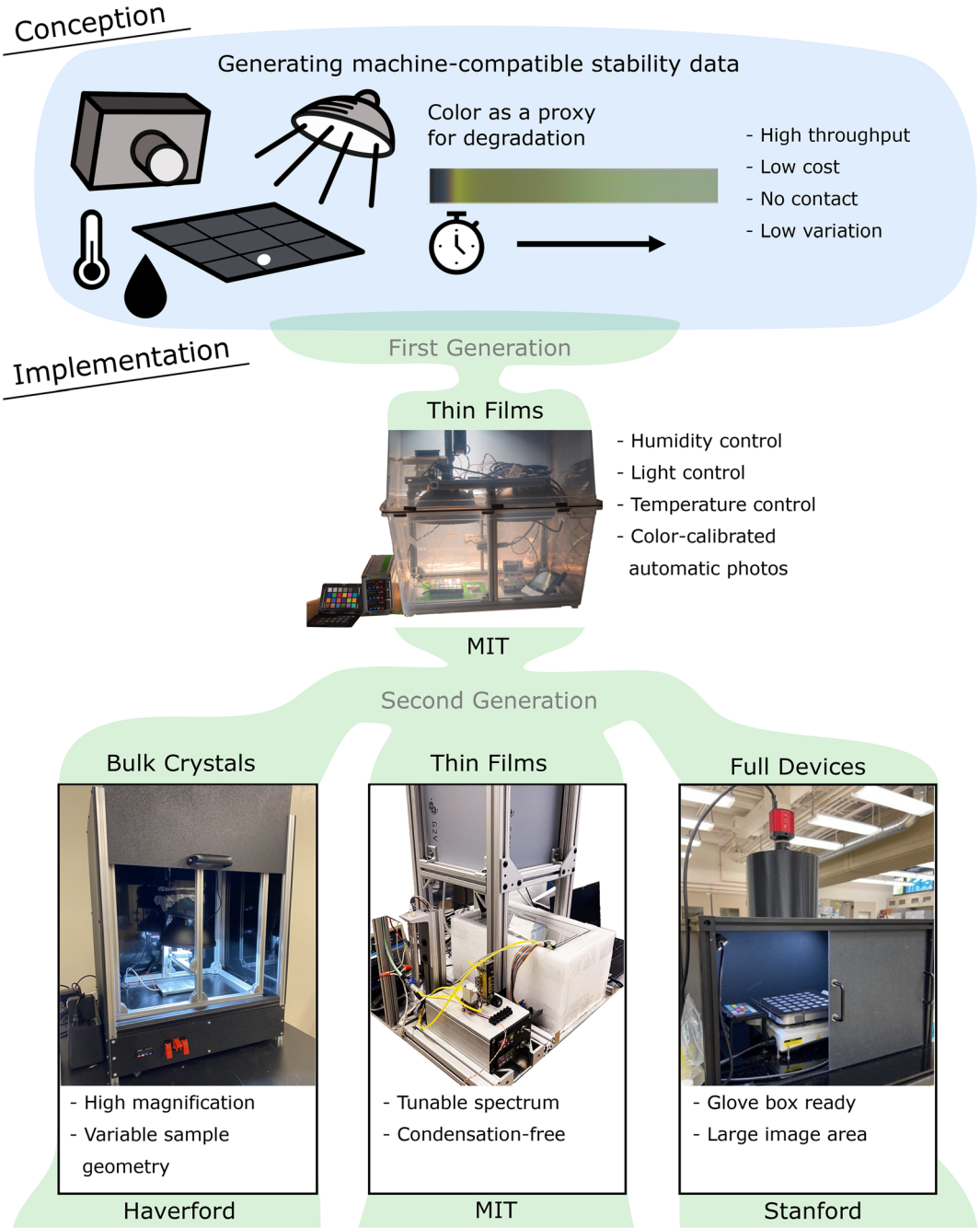


Fig. 1 Environmental chamber design and evolution.

of material instability. This approach can be applied to perovskite degradation because halide perovskites like methylammonium lead iodide ($MAPbI_3$) undergo phase transitions with distinct colors during degradation. By examining color change, we argue that it is possible to non-invasively monitor degradation kinetics in longitudinal perovskite testing.

### 2b. Color as a proxy for perovskite degradation

In this section, we present the optical proxy for perovskite stability based on the change of color. We establish correlations between perovskite color change and (1) solar cell device degradation for thin-film samples, and (2) changes in X-ray diffraction (XRD) patterns for bulk crystals. A combination of earlier results from the authors and new analyses is shown.

To establish trust in an optical measurement as a proxy for phase change, the limits within which optical proxies are valid are analyzed and possible false relationships identified. As the authors did not have access to an *in situ* XRD tool, we established the following correlations: (1) for ensembles of samples, we compared centroids of pre-degradation XRD data with the centroids of the time-resolved RGB-camera-based


© 2023 The Author(s). Published by the Royal Society of Chemistry

Open Access Article. Published on 13 February 2023. Downloaded on 1/29/2026 5:10:34 AM.
This article is licensed under a Creative Commons Attribution-NonCommercial 3.0 Unported Licence.

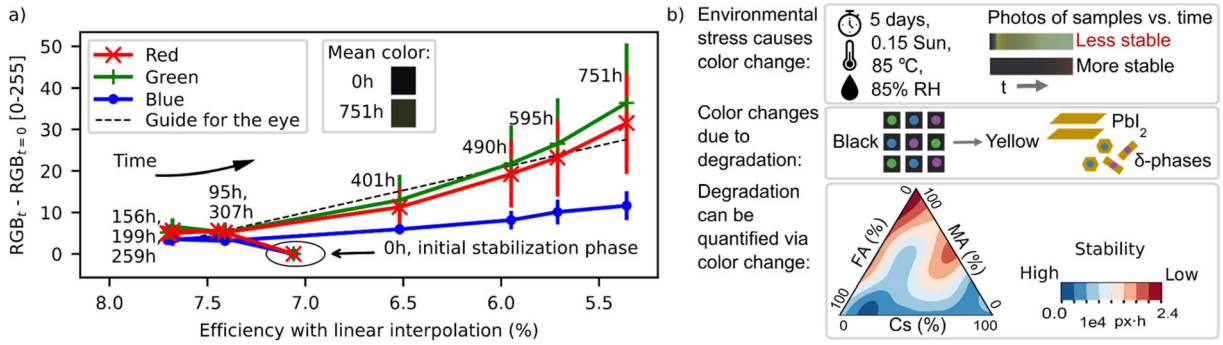


Fig. 2 (a) Evidence for the correlation between perovskite film color and device performance. Efficiencies and color changes were measured by Hashmi *et al.* in ref. 40. The colored patches represent the sample color before and after the aging test. The efficiency values shown here are linear interpolations to the time points of color measurements. (b) Color change in perovskite films can be used as a quantitative proxy for degradation, established by Sun *et al.*[43] Data in (a) reprinted and figures in (b) reprinted and adapted upon request to Journal of Materials Chemistry A and Matter, respectively.

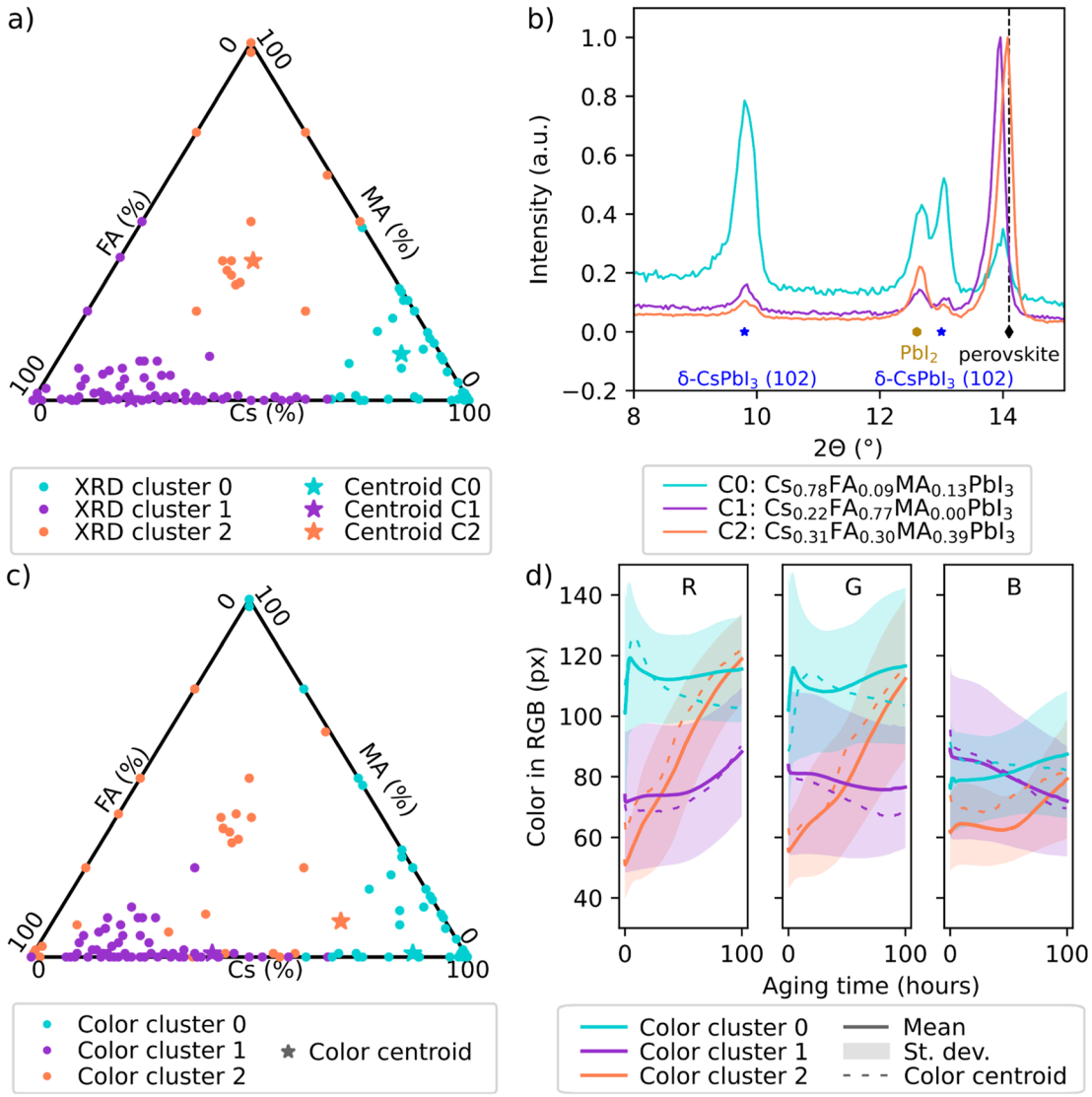


Fig. 3 Clustering comparison of initial structure and degradation of perovskite films (performed on $Cs_xMA_yFA_{1-x-y}PbI_3$ film samples degraded under heat, humidity, and illumination stress by Sun, Tiihonen *et al.* in ref. 43). (a) Clusters 0–2 identified from the X-ray diffraction spectra with (b) the spectra of the centroid samples C0–C2 with the most typical spectra shown. (c) Clusters 0–2 identified from the color degradation data with (d) the centroid samples with the most typical color degradation curves and the mean color degradation curves with standard deviations for each cluster shown. In (a) and (c), each dot is a perovskite sample. In (b), blue stars label δ-$CsPbI_3$, yellow hexagons $PbI_2$, and black diamonds α-mixed-cation perovskite phase.

Open Access Article. Published on 13 February 2023. Downloaded on 1/29/2026 5:10:34 AM.
This article is licensed under a Creative Commons Attribution-NonCommercial 3.0 Unported Licence.

measurements, using clustering methods to identify centroids (Fig. 3). (2) For individual samples, we measured XRD before and after degradation, and compared to color changes (Fig. 4). We also reference a prior study that examines changes in perovskite RGB color change with solar-cell device efficiency, shown in ESI Fig. S1.† The limits of this color-based proxy are explored in the last paragraph of this sub-section.

Evidence for $MAPbI_3$ perovskite film color serving as an indicator of perovskite solar cell degradation was directly established in Hashmi *et al.*[40] Evidence for correlation between the color and efficiency change is shown in Fig. 2a, with color change of the solar cells in Hashmi *et al.* shown as a function of their efficiency. Efficiency values in Fig. 2a are linearly interpolated due to the different time points of measuring efficiencies and colors, see ESI Section S1.† Color works as a proxy here, because one of the perovskite decomposition products, $PbI_2$, has a much larger bandgap (2.27 eV (ref. 41)) than the original film, $MAPbI_3$ (1.52 eV (ref. 42)). This results in the yellowing of lead iodide perovskites under environmental stress. The utility of the color proxy as a means to identify more stable perovskite compositions was demonstrated in a study by Sun, Tiihonen *et al.*[43] as shown in Fig. 2b: proxy measurements on bare films within the MA-FA-Cs lead iodide quasi ternary phase diagram—implemented using the first generation degradation chamber shown in Fig. 1—indicated a more stable composition centered at $Cs_{0.17}MA_{0.03}FA_{0.80}PbI_3$; it was 3× more stable than the reference state-of-the-art $Cs_{0.05}(MA_{0.17}FA_{0.83})_{0.95}Pb(I_{0.83}Br_{0.17})_3$ and yielded 30% less degradation in a damp heat test when tested directly at the device level.

A correlation between color and degradation is established within the limits that the decomposition products remain optically distinguishable from the original phase within the wavelengths defined by the equipment. Optical cameras with red, green, and blue channels (approx. 550–700 nm, 450–650 nm, and 400–550 nm, respectively, for commercial cameras but highly dependent on the camera model[44]) have reduced sensitivity for colors outside their spectral sensitivity area, *i.e.*, approximately below 1.78 eV. The spectral sensitivity range of commercial cameras can be extended to up to approximately 900 nm (1.4 eV)[45] by the removal of an integrated infrared filter from the camera. The spectral sensitivity of each setup should be measured because the camera lens and other components absorbing irradiation affect the result. For example, the mixed MA-FA-Cs lead iodide perovskites investigated in Sun, Tiihonen *et al.*[43] have a potential degradation route *via* dark minority-phase formation (*e.g.*, perovskite-structured $CsPbI_3$ suggested with computationally estimated bandgap of 1.57 eV (ref. 46)) in addition to decomposition of perovskite into yellow by-products. Thus, the infrared filter was removed from the

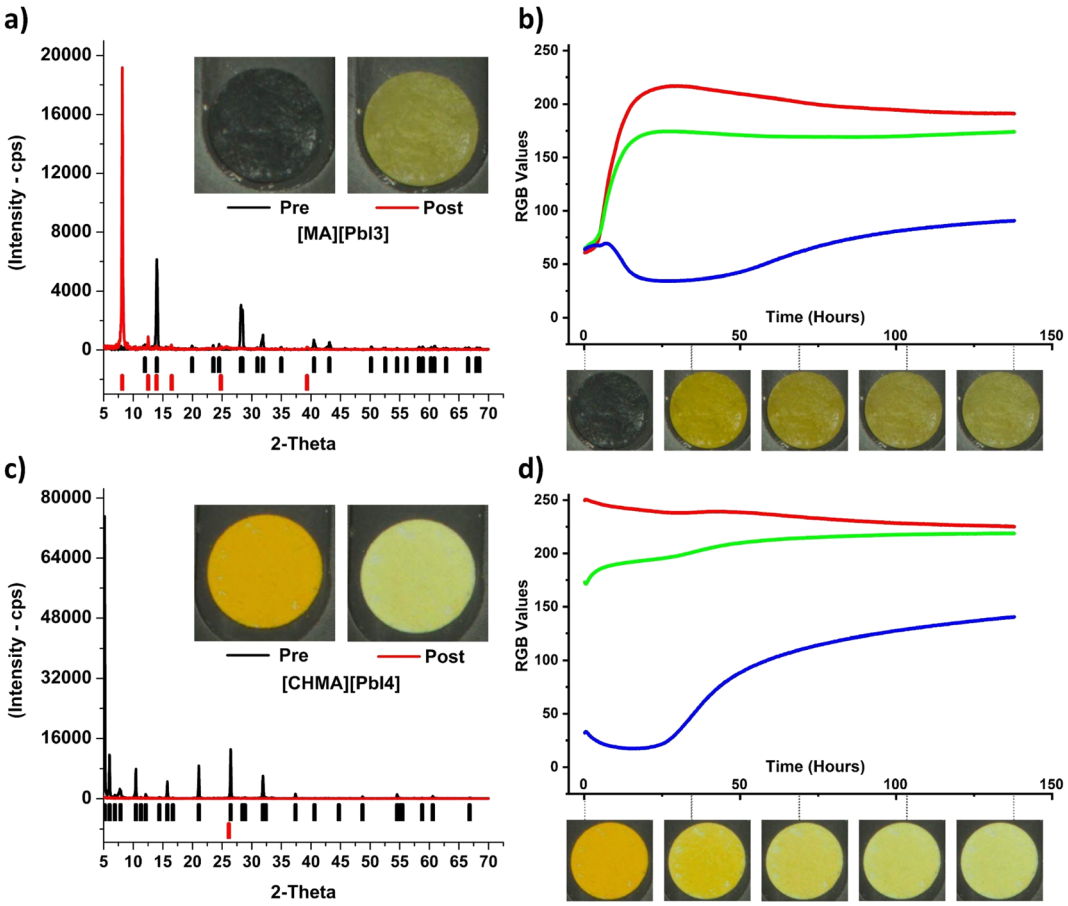


Fig. 4 (a) and (b) Pre/post powder XRD patterns and color change time-series for $MAPbI_3$, and (c) and (d) [CHMA][$PbI_4$] bulk samples.


© 2023 The Author(s). Published by the Royal Society of Chemistry

Open Access Article. Published on 13 February 2023. Downloaded on 1/29/2026 5:10:34 AM.
This article is licensed under a Creative Commons Attribution-NonCommercial 3.0 Unported Licence.

camera in the first generation MIT chamber (Fig. 1) to better avoid these dark-coloured "false positives".

Color change could potentially be a lagging indicator of device efficiency because, by the time the film color has noticeably changed, the concentrations of other defects (including point defects) may already be high enough to affect device performance. The precise amount of the lag depends on the point-defect chemistry, composition, and degradation pathways of the film. For the example shown in Fig. 2a and ESI Fig. S1,† the lag is less than 142 hours over a total test time of 800 hours. The comparison of the average colors of the samples before and after the aging test (Fig. 2a) indicates that also subtle color changes can be quantified by the color-calibrated photographing procedure. Generally, as long as the lag remains constant or has less variability than the change of degradation onset between the target and reference samples, the optical proxy remains useful.

This work aims at degradation data that can be used to run accelerated searches for more stable materials. For this purpose, a relevant proxy variable for degradation connects to perovskite structure across reasonable composition variations. Thus, we compared the XRD and color data from perovskite films that had been used to produce the stability landscape in Fig. 2b in the earlier work.[43] A clustering approach was selected to jointly analyze the varying MA-FA-Cs lead iodide compositions. We clustered all the XRD spectra of the non-aged perovskite films that had been collected from this compositional region during the work.[43] No composition information of the samples was used in this phase. We repeated the same clustering process on the optical data[43] from the same composition region. A hierarchical clustering approach was used for assigning a cluster to each normalized XRD spectrum or color time series in the two datasets (see Experimental for the detailed implementation).

Three clusters were identified for both datasets by a combined analysis of the hierarchical clustering dendrograms, silhouette score, and Davies–Bouldin index values (ESI Fig. S2 and Sections S5–S6†). Overlaying the XRD clusters atop the composition map (Fig. 3a) illustrates firstly a check that the algorithm is capable of recognizing meaningful compositional clusters of structurally resembling samples (indicated by the XRD spectra). The clusters would be spread randomly over the composition space if the clustering algorithm were not able to recognize relevant differences among the spectra. The same check holds true for the color clusters (Fig. 3c). Secondly, the comparison of Fig. 3a and c reveals that the clusters from the XRD and color data are very similar apart from some differences along the cluster borders (that should be regarded as approximate, as the sample properties transition softly instead of a full phase transition) and in high-MA region. The similarity of the clusters indicates that the perovskite film samples that have a similar structure when they are fresh samples (observed *via* XRD) experience similar color changes during degradation (observed *via* RGB color), and *vice versa*, an observation that strengthens the color proxy.

To understand the behavior of the clusters and to determine how the two maps differ, we analyzed the cluster centroid samples (here, the most typical XRD spectrum of a non-aged sample, Fig. 3b, or the color time series of a sample, Fig. 3d). All the cluster centroid samples were dark and similar in appearance to fresh samples (ESI Fig. S3†), nevertheless, they degraded differently (Fig. 3d and ESI Fig. S3†). The degradation of the perovskites *via* perovskite decomposition into $PbI_2$ is seen as yellowing. In RGB color representation, this means the blue RGB channel decreases relative to the green and red channels. The centroid of RGB cluster 2 experiences constant yellowing during the aging test (intermediate degradation). RGB cluster 1 retains color relatively well, with yellowing only in the end (the least degradation). In RGB cluster 0, there are rapid color changes in the first minutes of the aging test and then the mean color stabilizes to yellow color (the most degradation). The mean RGB data of these clusters (Fig. 3d) follow the same trends, as well as the RGB curves of the XRD cluster centroids (ESI Fig. S3†).

The distinctive degradation trends among the three clusters are explained by the initial structural differences between the clusters. In Fig. 3b, XRD cluster 0 centroid shows distinctive features from XRD cluster 1 and 2 centroids attributed to the high δ-$CsPbI_3$ content in cluster 0. δ-$CsPbI_3$ is an orthorhombic perovskite phase that is yellow and non-photoactive, and in high content it may even result in the film appearing yellow. This yellow phase is also an accelerator for α-perovskite degradation, possibly by acting as nucleation centers for decomposition.[43] This observation explains the differences in the high-MA region between the XRD and RGB clustering – both high-MA and high-FA samples turn yellow rapidly but the former turns yellow due to perovskite decomposition and the latter is aided by the presence of yellow δ-phase. In XRD cluster 1 sample, more Cs are incorporated into the α-mixed-cation-perovskite, and excess $PbI_2$ remains in the film. During aging, the incorporation of Cs into α-perovskite lattice is expected to improve perovskites' thermal stability, leading to a delay in the color transition between the black α-mixed-cation-perovskite and its decomposition product of yellow $PbI_2$. We note that the stabilization effect from Cs incorporation is counterbalanced by the accelerated degradation due to the presence of excess $PbI_2$. Finally, XRD cluster 2 sample shows combined features of the two other clusters. Higher Cs and lower FA in perovskite crystal structure in cluster 2 samples compared to cluster 1 is evident by the contraction of the cubic perovskite lattices, shown in the right-shifted (001) perovskite peak at around 14°. The increased MA content in XRD cluster 2 compared to cluster 1 leads to weakened moisture stability during aging tests, where the films are expected to turn from black to light yellow till transparent under high humidity. Cluster 2 also has increased δ-$CsPbI_3$ content compared to cluster 1. These differences among the XRD cluster centroids (also visible in the XRD spectra of the RGB cluster centroids, ESI Fig. S3†) are expected to lead to stability differences among the clusters: cluster 1 > cluster 2 > cluster 0. This is indeed in line with the observations from the color data. The degradation chambers presented in this work have the capacity to produce large amounts of data across large composition ranges with little manual intervention. The clustering approach can be

Open Access Article. Published on 13 February 2023. Downloaded on 1/29/2026 5:10:34 AM.
This article is licensed under a Creative Commons Attribution-NonCommercial 3.0 Unported Licence.

utilized for retrospectively analyzing the color degradation data from the degradation chambers presented in this work and guiding the in-depth analysis or further characterization to cluster centroids.

Next, the color proxy is extended to bulk samples in addition to perovskite film samples. In this case, device efficiency is not a direct useable metric, therefore changes in crystal structure are used to elucidate the extent of degradation. Powder XRD analysis was performed before and after longitudinal aging tests. Samples were aged for 150 hours at 0.15 Sun, 85 °C and 85% RH. As with thin film testing, image capture was performed at the visible wavelengths, with analysis of RGB channels.

Bulk crystals have a smaller surface-area-to-volume ratio than thin films. This means that degradation observed *via* optical change occurs at the surface of the sample but may not be indicative of subsurface structural change when the crystals are opaque. To address this limitation, crystals were ground and spread thinly across filter paper sample holders to ensure uniform degradation across the volume of the samples and increase the kinetics of degradation.

The complete reduction in peak intensity in the [CHMA][$PbI_4$] crystals (Fig. 4c) shows that Bragg's law no longer holds; the samples are no longer crystalline after the degradation test. In the $MAPbI_3$ samples, the shifts in peak intensity illustrate the change to another crystalline structure (Fig. 4a). These changes lead to distinct color change patterns of the samples during the degradation test (Fig. 4b and d).

In summary, calibrated color change is established as a reliable proxy for degradation in perovskite bulk samples, thin films and solar cell devices, and has aided researchers to improve perovskite device stability. This proxy is valid within the following limits: (1) the decomposition phases are optically distinguishable from the original sample at the wavelengths selected for the hardware (light source and imaging system), (2) the lag between color change and device efficiency decrease is sufficiently small, and (3) bulk samples have a sufficiently large surface area to volume ratio such that surface degradation is representative of overall degradation.

## 3. Implementations

### 3a. First generation chamber at MIT (thin films)

The MIT Environmental Chamber Gen. 1 (Fig. 5) is designed for high-throughput degradation testing of perovskite films with areas of approximately 1.27 × 2.54 $cm^2$. Color change is used as a proxy for degradation which is induced by environmental stress from the heated sample holder (up to 100 °C), increased air humidity (up to approximately relative 85% air humidity depending on the level of heating), and illumination (up to 0.16 Sun visible light). Calibration data for the chamber is available in the open access documentation repository supplementing this article (see Data and code availability statement). The chamber is easily expandable for higher-throughput testing. It can fit 28 thin film samples under each camera-lamp pair and at maximum two pairs of lamps fit into the chamber. The components are chosen primarily so that they are widely and readily available with reasonable cost, and can be adapted apart from the main parts (the lamp, camera, lens, and reference color chart shown in Fig. 5). Therefore, this version of the chamber serves as a straightforward path for implementing automated aging testing capacity for any laboratory willing to expand towards stability research. The cost range of this version of the chamber is US$2000–$5000 depending on the amount of reused materials utilized in the process.

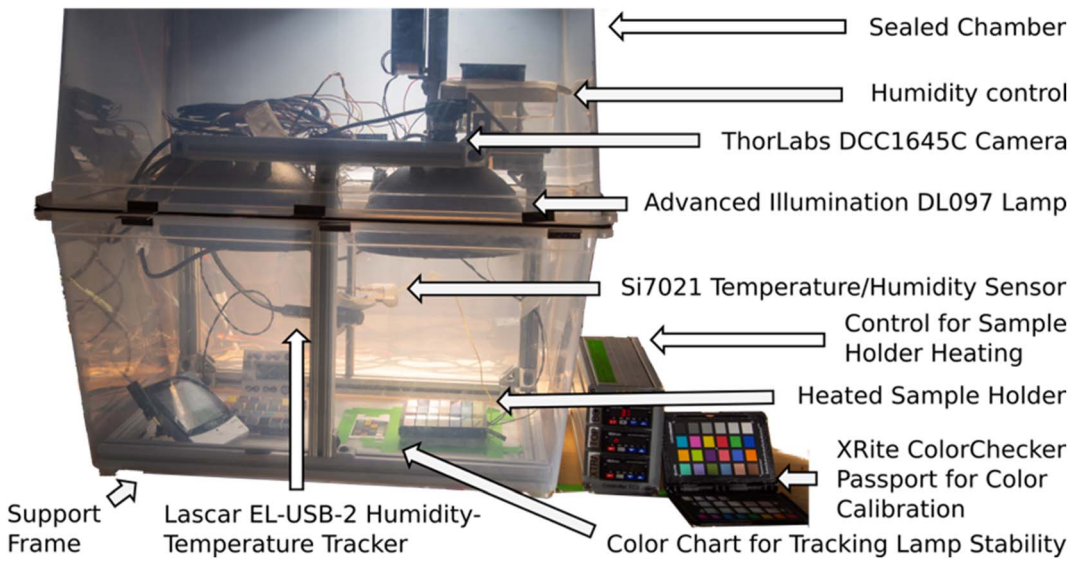


Fig. 5 The MIT Aging Chamber Generation One with the main components identified. Excluded from the image are a control laptop, Arduino humidity controller, and a darkening curtain that is placed on top of the chamber when the chamber is running. The LED lamp is ring-shaped and has a conical shade to produce even illumination to the 4 × 4 $inch^2$ sample holder area. The humidity is controlled by evaporating water with a fan, and additional fans even out the humidity and temperature across the chamber. Two lamp-camera-sample-holder combinations fit into the chamber that is sealed with an insulation band and clips.


© 2023 The Author(s). Published by the Royal Society of Chemistry

Open Access Article. Published on 13 February 2023. Downloaded on 1/29/2026 5:10:34 AM.
This article is licensed under a Creative Commons Attribution-NonCommercial 3.0 Unported Licence.

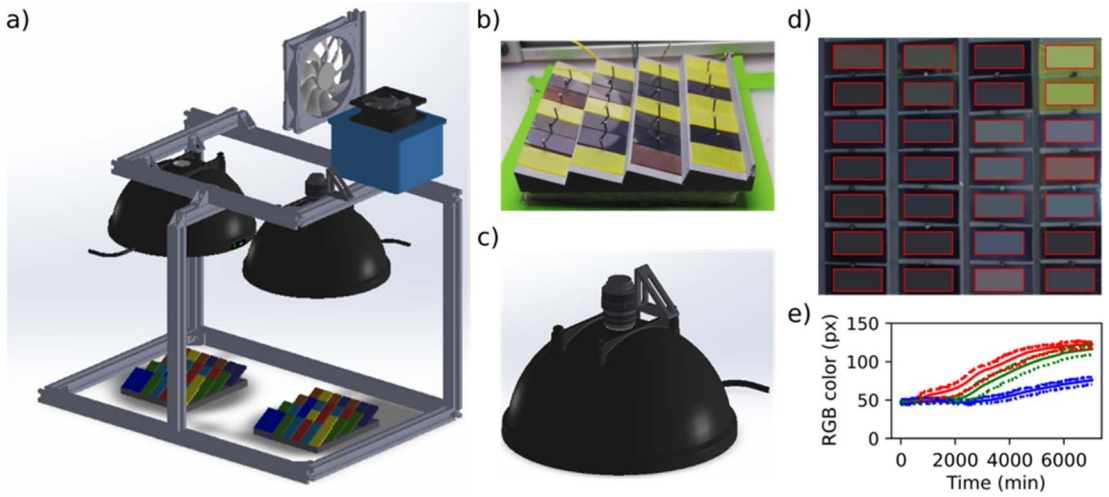


Fig. 6 Construction of the MIT Generation One Chamber. (a) Support frame with lamps, cameras, and evaporative humidity control system attached. (b) Graphite sample holder loaded with high- and low-Cs content perovskite film samples. (c) The programmable camera is positioned to look at the samples through a hole in the conical shade of the lamp. (d) Python analysis script crops the image to the sample holder area, slices it to pieces containing the interior of each sample, averages the color and color calibrates it. (e) Average red, green, and blue (RGB) pixel color of an exemplary perovskite sample over the aging test duration.

The structure of the main parts within the chamber is illustrated in Fig. 6a (detailed description in the documentation repository, see Data and code availability statement). The humidity of the chamber is controlled *via* an Arduino-driven stand-alone software (shared in the code repository, see Data and code availability statement). The sample holder temperature is controlled with a resistive heater – thermocouple pair. The chosen LED lamp is stable enough to be used with a fixed operation voltage during aging tests with durations from days to few weeks. In addition to the controls, the chamber includes a separate high accuracy air temperature and humidity logger as well as a feature for detecting possible lamp failures or lamp aging retrospectively from the image data (described in the documentation repository). The building block design presented above facilitates implementing only the necessary parts of the chamber when the design is adapted for future applications.

The sample holder (Fig. 6b) is made of graphite to conduct heat efficiently and is painted with matte, neutral gray paint to avoid interfering with sample photography. Pins are used for mounting the samples accurately on the sample holder, and the surfaces are tilted to reduce specular reflectance of the perovskite film samples. The sample degradation during the aging test is monitored *via* a ThorLabs DCC1645C CMOS camera that is attached to the lamp dome (Fig. 6c). The camera was ordered from the manufacturer with the infrared filter removed, in order to expand the spectrum of the camera. The camera is controlled with a LabVIEW program (shared in the code repository) in which the main camera settings can be adjusted according to the illumination conditions and the frequency of taking pictures is set. Additional electric contacts can be added to the sample holder for expanded *in situ* characterization but are opted out in this chamber version. This is because a minimum design producing data for machine learning -aided high throughput aging testing was desired, *i.e.*, the priorities were simplicity, expandability and data with machine-readable quality with minimal interventions.

Image data is analyzed after the aging test with a Python script (shared in the code repository). Due to the consistent shape of the samples, the script is designed to crop the images to the sample holder only, slice them to single sample sub-images, average the color over the sample, and color calibrate them (a result from the script analysis is shown in Fig. 6d). The color calibration is a crucial step in producing repeatable and reproducible color data. It is performed by the aid of XRite ColorChecker Passport (Fig. 5). The ColorChecker is photographed in the chamber in the place of the sample holder as the first image of each aging test, and used as a reference. The difference between how the color of each color patch is known to appear under a D60 reference illuminant and how they are observed by the camera in the aging chamber is used as a basis for calibrating the colors of the samples. The color calibration is implemented *via* a 3-dimensional thin plate spline transformation from the color space of the chamber to the reference color space, first transforming the colors from RGB color space to LAB color space, then applying the spline transformation, and transforming back to LAB color space. The approach is described in detail in the ESI† of our previous work[43] and the code implementation is integrated into our analysis script (shared in the code repository). The Python script applies the color calibration automatically to all but the first picture in the aging test data folder and produces graphs on the average color-calibrated sample color as a function of the aging test duration (Fig. 6e).

### 3b. Second generation chamber at Haverford (bulk crystals)

The design principle of the Haverford Group's Aging Chamber (Fig. 7) is to optimize image capture with bulk-crystal perovskite

Open Access Article. Published on 13 February 2023. Downloaded on 1/29/2026 5:10:34 AM.
This article is licensed under a Creative Commons Attribution-NonCommercial 3.0 Unported Licence.

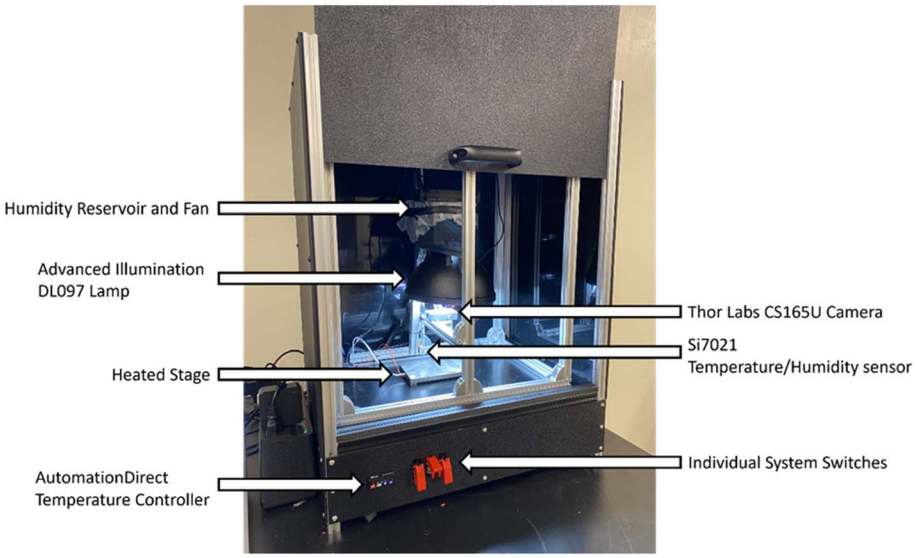


Fig. 7 The Haverford Environmental Chamber, for measuring bulk crystalline samples, with key componentry labeled.

samples. Bulk-crystal samples have variable geometry, positioning on the substrate, and a smaller absolute, observable surface area compared to thin films. The samples in this chamber are placed in nine separate wells, allowing for the simultaneous testing of up to nine different samples. The surface area of the bulk crystal samples ranges from 0.5–1.5 $cm^2$. To adapt the chamber to the specific workflow and sample type, the image acquisition software was modified along with the sample heating/holding assembly, and chamber enclosure, while keeping most of the hardware choices in the first generation chamber. Minor changes were made in terms of hardware placement, microcontroller choice, electronics storage, and data acquisition scripts to suit lab operators' preference.

**Hardware changes.** The Haverford aging chamber uses the same lighting, image acquisition, humidity control, and heating hardware as the first generation chamber. However, image acquisition of smaller samples (necessitating a shorter focal length and higher magnification) is more sensitive to

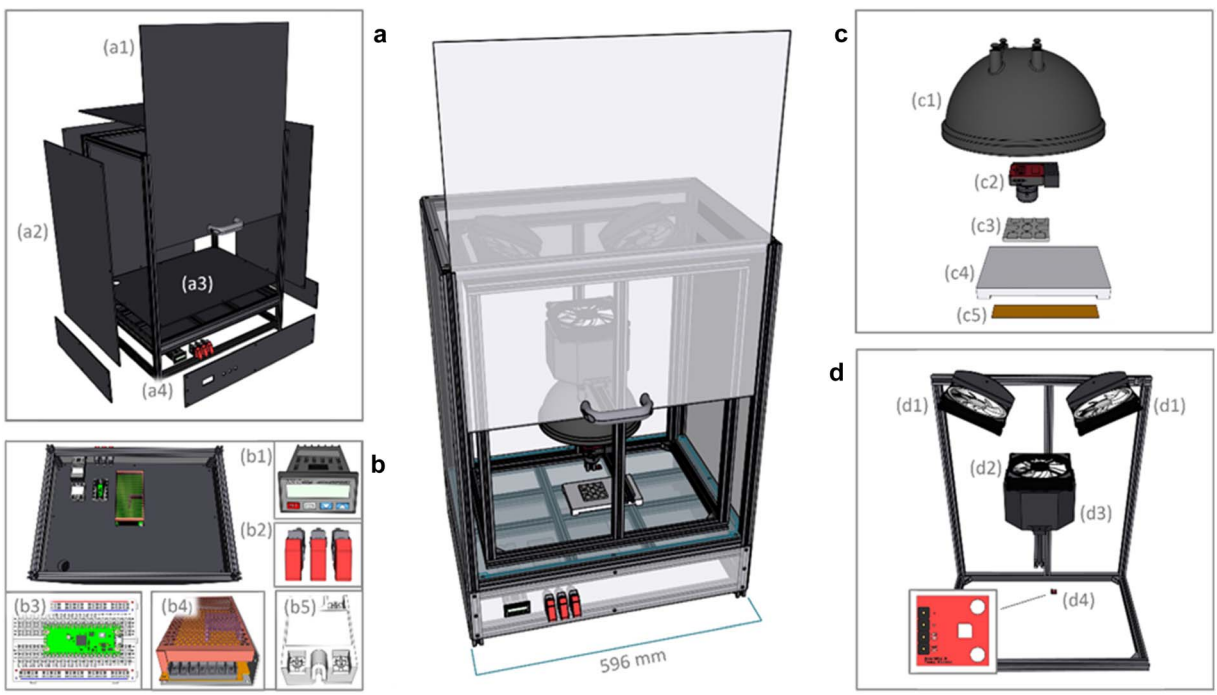


Fig. 8 An overview of the Haverford Environmental Chamber, and the modified systems. (a) The chamber enclosure. (b) The electronics compartment (from bottom), and electrical components. (c) The imaging/lighting system, and the sample heating system. (d) The humidity-control system.


© 2023 The Author(s). Published by the Royal Society of Chemistry

Open Access Article. Published on 13 February 2023. Downloaded on 1/29/2026 5:10:34 AM.
This article is licensed under a Creative Commons Attribution-NonCommercial 3.0 Unported Licence.

refraction from changes in ambient temperature within the chamber. As the chamber comes up to temperature, the image from the camera distorts due to the changing temperature gradient in the air. Hardware modifications were made to reduce air temperature fluctuations within the chamber. The chamber needed to be preheated to stable operating temperature before samples were loaded and to return to thermal equilibrium quickly after loading. To accomplish this, the Haverford chamber has a different enclosure Fig. 8a with a vertical sliding door to reduce temperature loss when loading Fig. 8a1, and a heated stage with high thermal mass Fig. 8c4 to minimize the temperature dip when the sample holder Fig. 8c3 is added.

The Haverford Chamber's enclosure Fig. 8a is built from aluminum extrusions and ABS paneling Fig. 8a2. The floor of the chamber is a G10–FR4 fiberglass-epoxy laminate panel ("Garolite") Fig. 8a3 to withstand the heated stage without warping. The chamber is sealed with sealant tape compressed between the panels and the aluminum extrusions. The opacity of chamber walls eliminates the need to account for external lighting fluctuations. The underside of the enclosure contains a separate compartment Fig. 8a4 and b used to mount and organize the electrical components: Raspberry Pi Pico and breadboard Fig. 8b3, power supply Fig. 8b4, AutomationDirect temperature controller Fig. 8b1, toggle switches, Fig. 8b2, and solid state relay Fig. 8b5.

Modifications were made to the placement of circulation fans Fig. 8d1, so that air flow to the sample stage does not shift the samples during image acquisition. The water reservoir is 3D printed Fig. 8d3 to mount to the chamber frame and press fit with the humidity control fan Fig. 8d2. The SI702 temperature/humidity sensor Fig. 8d4 is mounted on an aluminum extrusion close to the heated stage. The chamber uses the same Advanced Illumination DL097 lamp Fig. 8c1 as the MIT Gen. 1 design. The ThorLabs CS165CU camera is lowered Fig. 8c2 closer to the sample holder, and the focal length of the lens (ThorLabs MVL6WA) is adjusted to increase magnification. The total hardware cost for the Haverford chamber is estimated at US$2500.

**Software changes.** Haverford chamber uses calibrated color change in perovskite crystals as a measure of their instability. Bulk crystalline samples require a new image analysis pipeline to extract degradation data because (1) they are smaller than the thin films analyzed in the first generation chamber, (2) they do not entirely fill up the sample holder, and (3) their exact locations are variable. To address this challenge, the Haverford chamber has an automated image acquisition pipeline implemented with OpenCV in Python. This pipeline uses computer vision to automatically isolate single crystal samples from the captured images and

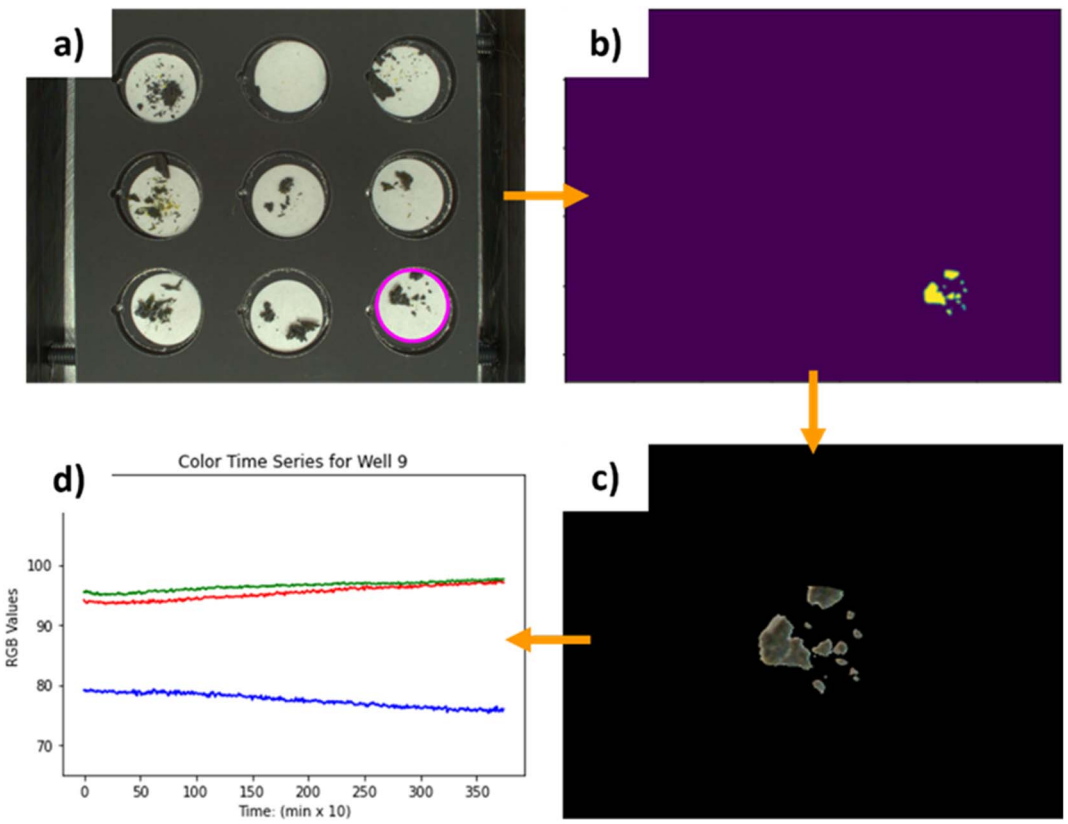


Fig. 9 The image processing pipeline of the Haverford Gen. 2 chamber. (a) First, a region of interest containing the desired sample is isolated from the raw image. In this case, the samples in well 9 (bottom right corner) are selected. This is done using the Hough transform circle detection on the white filter paper underneath the samples. (b) The known color of the filter paper (acquired from a "blank" well without any samples) can be used as a green screen to remove all the filter paper pixels. This leaves a mask that leaves only the samples. (c) This mask is then applied over the original image. (d) The RGB values of the isolated samples can then be analyzed.

Open Access Article. Published on 13 February 2023. Downloaded on 1/29/2026 5:10:34 AM.
This article is licensed under a Creative Commons Attribution-NonCommercial 3.0 Unported Licence.

extracts their color change in RGB values over time (Fig. 9). This process is very useful for small samples, as the chamber can isolate them from the scene and mask the extraneous pixels.

This image processing is adaptable to other samples of variable geometry. The only features the image isolation relies on are circular filter paper, and sufficient contrast between the sample and the paper. Any bulk sample that is placed on filter paper with enough contrast can be automatically isolated from the rest of the image, and its color changes extracted. This also demonstrates that software can be treated as another sub-module of the chamber and varied independently from the rest of the design for an adopter's specific use case.

To fit the scripting preferences of the Haverford operators, the original Arduino Uno was replaced with a Raspberry Pico running MicroPython. The Pico controls the humidity fan, and the two chamber circulation fans. All fans are 140 mm, powered by a 12 volt line and mounted to the aluminum frame with 3D-printed mounts. Data acquisition scripts were written in Python on the data-logging computer to compile data from the Solo 4824 temperature controller, the Si7021 temperature/humidity sensor, and the ThorLabs CS165CU camera and save them to a specified experiment file.

### 3c. Second generation chamber at Stanford (full devices and modules)

The Stanford Environmental Chamber is designed specifically for imaging heat-based degradation of full solar devices as well as perovskite films produced *via* the rapid spray plasma processing (RSPP) method.[47] Additionally, the chamber can compare devices produced with other common fabrication techniques like spin coating with RSPP perovskite films. The chamber maintains RGB color as a means to characterize thermal degradation pathways in the perovskite thin-film solar devices similar to the first generation chamber; however, to exclude other degradation pathways, the chamber is constructed to be assembled in a glove box under nitrogen atmosphere and fully enclosed to prevent light impingement from external sources (windows, glove box lights, room lighting, *etc.*). The heat is applied directly to the films placed against a hotplate at the accelerated degradation temperature (generally 85 °C).

The Stanford perovskite films and devices encompass a variety of small cells, mini-modules, and module architectures necessitating a large imaging stage capable of fitting multiple devices simultaneously. A flat hotplate rather than the inclined substrate used in MIT's work was selected as the imaging platform to accommodate the varying perovskite films and device architectures with ease. Rather than placing the camera within the light source as is the case with the MIT Gen. 1 chamber, the camera is outside the chamber to protect the electronics *via* passive cooling along with providing a large field of view. The lighting sources are placed within the box at angles to minimize glare and reflection into the lens shown in Fig. 10a. A maximum of 36 2 × 2 $cm^2$ cells and a variety of module architectures can comfortably fit on the hot plate surface as is demonstrated in Fig. 9c and 10b, respectively. Due to the need

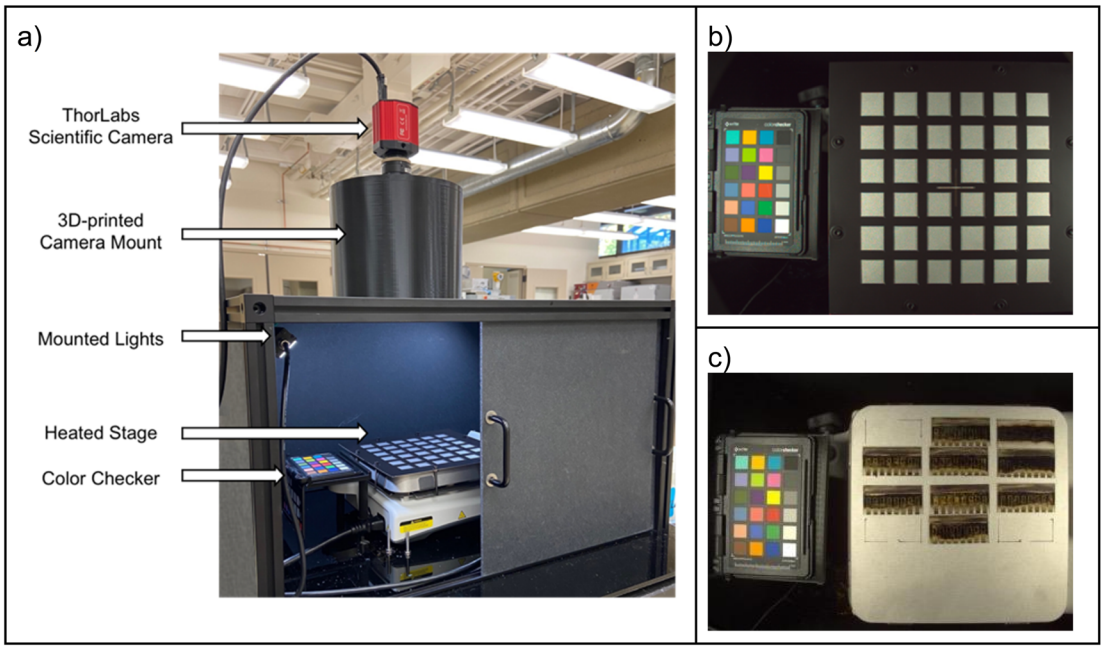


Fig. 10 (a) The Stanford Enclosed Environmental Chamber composed of an illuminated and heated stage, XRite Color Checker, and mounted optical camera (ThorLabs CS126CU and MVL12M1). (b) The aligned 6 × 6 grid for imaging small solar cells. (c) An example of RSPP module architectures on the imaging stage. The Stanford system analyzes the passport Color Checker with each image, as the system has a large illumination and imaging area of capture, allowing one to track and normalize color values against the checker along with following absolute drift in RGB values of the Color Checker between batches. Photobleaching of the Color Checker is a particular concern over thousands of hours of use and can be tracked using this approach because the checker remains in the field of view in each image. Additionally, this system can be run in two modes: continuous illumination and illumination only for photograph capture (flash mode). The two modes allow for a mitigation of device photodecay with flash mode and accelerated device photo-aging in the fully illuminated mode.


© 2023 The Author(s). Published by the Royal Society of Chemistry

Open Access Article. Published on 13 February 2023. Downloaded on 1/29/2026 5:10:34 AM.
This article is licensed under a Creative Commons Attribution-NonCommercial 3.0 Unported Licence.

for a high uniformity hotplate coupled with the large field of view quality optics, the total price of the Stanford Environmental Chamber is estimated at US$7000. Cost reductions can easily be achieved with lower-resolution optics (from 12.3 MP to 1 MP) that still allow for quality cell imaging.

### 3d. Second generation chamber at MIT (thin films)

Similar to the first generation chamber, the MIT Generation 2 Chamber (Fig. 11) is designed for high-throughput characterization of perovskite films and other oxygen-sensitive materials. However, the MIT Second Generation Chamber is designed specifically to have precision control of the dew point, which facilitates performing long aging tests with very high humidity levels. The chamber is integrated with a commercial solar simulator instead of an LED lamp in order to extend illumination intensity to up to 1 Sun, and to add spectral control. These features extend the chamber's capabilities for degrading durable perovskite materials and, due to 1 Sun visible illumination source, are also more compliant under consensus stability testing conditions for perovskite solar cells.[15] This second generation chamber is designed to cost less than US$1500. The implementation of a commercial solar simulator for increased range and fidelity comes with an increase in chamber cost (approximately US$7500 with the solar simulator at the time of assembly). However, this price still remains in the low range in comparison to those of commercially available degradation chambers.

The chamber is illuminated with a G2V Sunbrick class AAA solar simulator with 625 $cm^2$ illumination area and a spectrum that is adjustable between 400–700 nm. The simulator is controlled with software provided by the manufacturer. A moisture-controlled environment is attained within MIT Generation 2 Chamber through a double enclosure system where the outer enclosure is filled with water to fully submerge the inner chamber. Naturally, air within this enclosed chamber approaches its maximum saturation dew point, however, by piping dry nitrogen into the environment, the relative humidity of the air is lowered to control the dew point. Additionally, by having the chamber fully submerged in water, the temperature can be precisely controlled due to the high heat capacity of water.

The external chamber is open on the top and has a sliding lid to minimize water evaporation while the internal chamber is open on the bottom to the moisture-controlled air environment. The internal chamber is submerged into the water-filled external chamber and the upward buoyancy force is overcome by securing the internal chamber underneath a set of plastic rails, shown in Fig. 12a. Water is continuously circulated within the system using a peristaltic pump *via* a water tube, illustrated in Fig. 12b, to both regulate the internal temperature and empty excess water from within the internal chamber air cavity. The temperature of the internal sample environment is controlled by the water temperature, which is regulated by an immersion heater and programmable controller. A dry nitrogen line runs in tandem with the water circulation line to control the relative humidity of the internal chamber by releasing dry nitrogen into the base of the internal chamber where the air cavity is located within the submerged enclosure. A base plate that holds the sample above the water line, shown at the bottom of Fig. 12c, has a sealable door that opens when a fan, shown in Fig. 12e, is

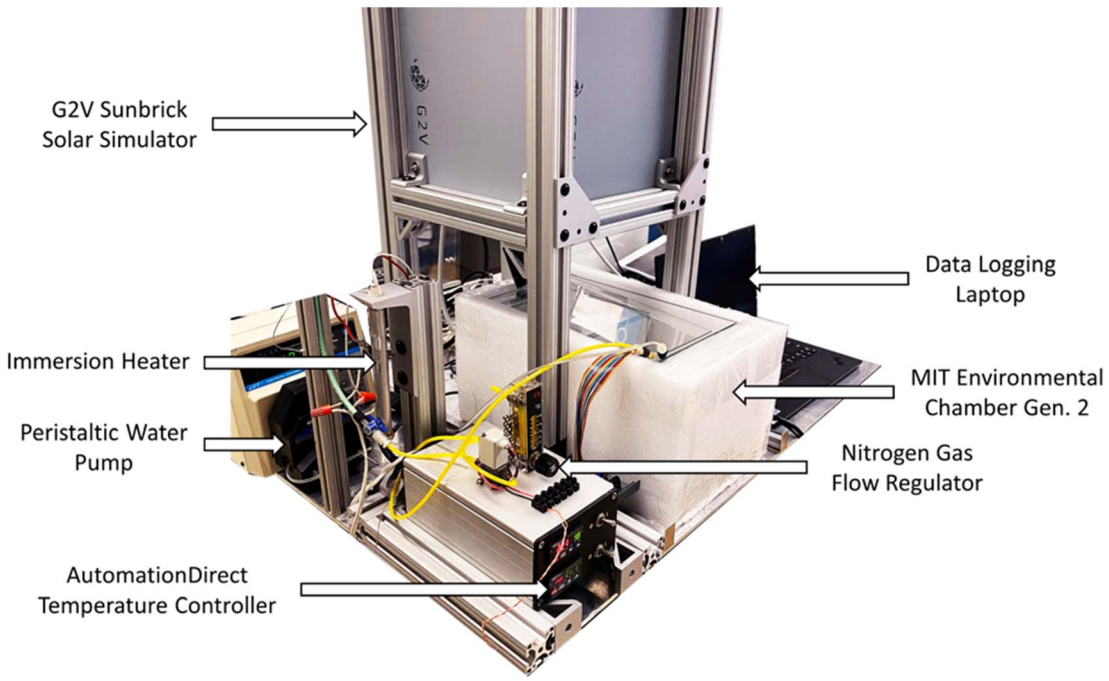


Fig. 11 The MIT Environmental Chamber Gen. 2 setup. The setup for the chamber consists of an LED solar simulator, immersion water heater, peristaltic water pump, water temperature controller, nitrogen gas flow regulator, and a laptop to log data. A styrofoam casing shields the sides of the environmental chamber to minimize uncontrolled temperature and lighting fluctuations.

Open Access Article. Published on 13 February 2023. Downloaded on 1/29/2026 5:10:34 AM.
This article is licensed under a Creative Commons Attribution-NonCommercial 3.0 Unported Licence.

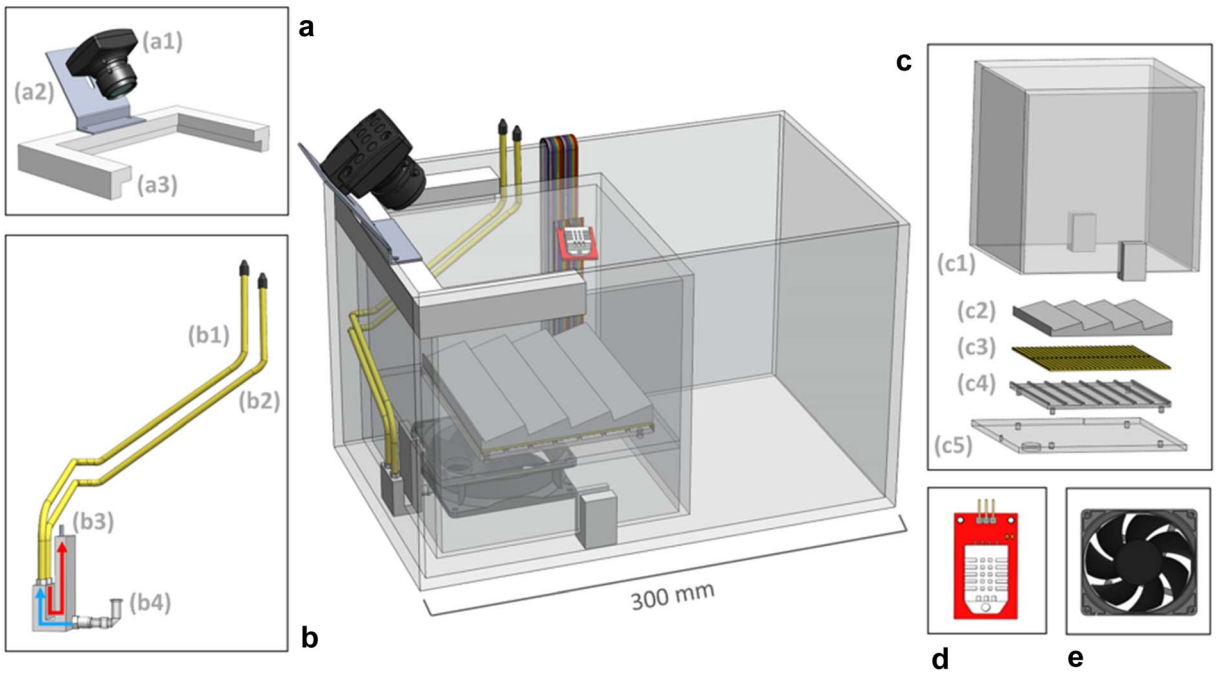


Fig. 12 The MIT Environmental Chamber Gen. 2 construction. (a) (a1) A ThorLabs camera is mounted to (a2) a rail bracket for imaging the samples in a fixed position. The camera and bracket are affixed to (a3) plastic rails that push against the top of the submerged internal chamber to counteract the upward buoyancy force created by the air cavity. (b) The plumbing system consists of (b1) a water circulation line and (b2) a nitrogen gas line. Dry nitrogen gas is added to the internal environment to lower the relative humidity through (b3) the gas outlet, following the red arrow. The water level is regulated by siphoning water out of the chamber through (b4) the water inlet, following the blue line. (c) The internal chamber that is fully submerged in water consists of (c1) a five-sided enclosure with an opening at the base and plastic grippers to allow for water to freely flow under the enclosure, (c2) an angled sample holder, (c3) a thermoelectric device to heat the sample holder, (c4) an acrylic mount, and (c5) a base plate with a sealable opening that allows for air circulation within the enclosure when a fan is activated. (d) A PCB temperature and humidity sensor mounted within the internal chamber with insulated wires feeding through the base of the internal chamber and out the top of the external chamber. (e) A circulation fan used to flow air from the moisture-controlled environment below the internal chamber into the sample environment enclosure.

activated to allow airflow into the chamber. The relative humidity of the sample environment is precisely controlled by tuning the flow rate of dry nitrogen into the air cavity and by circulating moist air from the water surface into the sample environment.

Samples are mounted on the sample plate, shown in Fig. 12c, at an angle normal to the camera line of sight. A ThorLabs DCC1645C CMOS camera (with an infrared filter removed from it) is mounted statically to a rail above the internal chamber to image the samples. A Color Checker card is placed inside the internal chamber to calibrate the camera color settings. A quartz disk is placed on the top of the chamber in the aerial transmission pathway from the samples to the camera to minimize optical aberrations due to the chamber material and water. The sample base plate has a thermoelectric module installed underneath to provide the option of directly heating the samples *via* conduction, as in the first generation chamber. A sensor, shown in Fig. 12d, is mounted within the internal chamber to control the temperature and relative humidity of the internal environment. Additionally, a separate humidity–temperature tracker is used for tracking the chamber conditions, as in Gen. 1 chamber. The culminating design of the MIT Environmental Chamber Gen. 2 gives researchers better control over high-throughput materials degradation experiments in extreme humidity conditions through the precise programming of dew point, temperature, relative humidity, and illumination spectrum within the sample environment.

## 4. Reflections and key learnings of this open-hardware effort

The four chambers described in this work are a part of an evolutionary-design process with two distinct generations of chambers. The process provides useful insight for scientist-developers who wish to share their hardware designs efficiently yet impactfully.

This hardware disseminated and evolved organically, even accidentally. Generation 2 hardware adopters were motivated by the scientific results obtained using the Generation 1 tool, and the offer to translate the technology within the context of ongoing government-funded research projects. When developing the chamber, establishing the validity of the color change proxy was essential in encouraging hardware adoption on the other sites. In Free Open Source Hardware (FOSH) literature, this step can be likened to proof of concept and validation, where the utility of a design is firmly established, and its


© 2023 The Author(s). Published by the Royal Society of Chemistry

Open Access Article. Published on 13 February 2023. Downloaded on 1/29/2026 5:10:34 AM.
This article is licensed under a Creative Commons Attribution-NonCommercial 3.0 Unported Licence.

functionality proven.[48] In our case, the MIT team devoted the upfront cost to establish the color change proxy through prior research, which formed the foundation of the aging chamber's experimental utility.[40,43] While this proxy was developed in thin-film devices, the confirmed utility encouraged other sites to implement the same experimental design in other sample types. The Stanford and Haverford sites evolved the hardware toward solar-cell devices and bulk crystal samples, respectively. This expanded catalog of known use cases makes it easier for further groups to adopt the hardware in the future, and establishes a rigorous, peer-reviewed foundation for further researchers to reference, motivating the Generation 1 and 2 tool-builders to document their work.

In transferring open hardware between sites, we found that "champions" of the technology-transfer process are integral at both the "push" and "pull" sites. These key figures facilitate the knowledge transfer, and actively communicate to modify the technology for the pull site's successful adoption. Even with thorough documentation, motivated contact persons at each site greatly facilitate implementing new use cases. At the "push" site, the champion acts to disseminate information on the build process, direct adopters to the relevant source material, and answer any remaining questions. At the "pull" site, the champion leads the effort in sourcing, building, and modifying the hardware for the specific application. While there is significant upfront cost involved at the pull site with transferring and adopting technology, user development has been recognized by other proponents of free open source hardware as a key advantage over traditional hardware by ensuring proper functionality for specific use cases.[49] Generally, we found that funded collaborations are more successful at technology transfer than unfunded collaborations.

During technology transfer, a regular line of communication between all the active sites was essential to avoid duplication of effort, and to expedite adoption. The contact at the "push" site can nurture parallel collaboration between "pull" sites. As an example, the aging chamber's enclosure at Haverford was replicated from observations of the Stanford group's design. The improved enclosure increased the rate of preheating and decreased heat loss from sample loading. These types of improvements would have been more commonplace had there been an organized community of adopters who would expand the library of use cases for open hardware and act as another source of information.[50] Such a community is common-place in developer and maker culture and would reduce the burden of the push sites to support multiple adopting labs.[51,52] In moving to share hardware with larger groups, we emphasize that an active community can crowd-source the time cost of supporting open hardware.

Resistance to knowledge drain from moving researchers is integral to ensuring longevity. A common flaw of purpose built laboratory equipment is that the knowledge to operate, maintain, and assemble the devices resides with the researchers that develop them. In academic settings, this issue is compounded by the movement of researchers to other institutions. We found that in a large project like this, knowledge is decentralized across multiple individuals. While decentralization is a major asset of open hardware,[53] we found that it can provide a share of difficulty. The process of tracking down knowledgeable parties further complicates adoption by other sites. The knowledge drain and decentralization can be combated by a robust repository for all supporting files and documentation—even the beta phase documents. Storage in shared drives can be a liability; shared drive transferring issues and managing permission adds unnecessary complications with transferring between researchers and with dissemination. Even if a project begins organically with files stored internally, it is worth investing time in a robust, easily accessible file storage system like GitHub.[54] Community repositories not only allow the easy sharing of hardware assets and operational knowledge, but also motivate the push and pull site champions by providing a formal route for referring to their work, and leverage the combined knowledge of multiple adopters. Multi-modal information transfer, including videos and photos, helped improve efficiency and accuracy of communication. Of course, having a lab manager or research staff involved further supports knowledge permanence.

Thorough documentation is the most important aspect for knowledge transfer and forms the backbone of adoption. The minimum viable package in our experience includes a comprehensive bill of materials, a library of standardized file types for 3D models, a thoroughly commented codebase, manual, and a permanent repository. It will be the first point of contact that pull sites will use, and will mitigate the effort needed at push sites to support other groups. For potential adopters, a thoroughly documented repository inspires confidence that the open source hardware is well supported, maintained, and achievable to build. To that end, to foster dissemination, hardware design should assume the lowest common denominator in mechanical experience and machine shop support at adopters' sites. This experience is in keeping with other established design philosophies of open hardware.[48] Using aluminum extrusions and other readily available pre-fabricated parts minimized the necessity for custom hardware and machining in this work. The use of consumer level electronics, like those available from Adafruit and Sparkfun both lowers cost, and reduces reliance on proprietary software.[55,56]

Facilitating hardware evolution allows cumulative improvements and branched applications that the initial developers could not anticipate. While it is likely beneficial to maintain a base version of the hardware like in a typical open-source code repository, in this work, we observed an added benefit from the branches that may evolve far from the baseline design and cannot be readily merged with it. From this viewpoint, creating simple community standards for documenting and sharing the work is more essential than investing on standards for adding features to the baseline design. In some cases, the latter approach can actually be prohibitive for the evolution process. The evolution can be further facilitated by thorough documentation, and open communication between sites on the strengths and weaknesses of the existing design.

Open Access Article. Published on 13 February 2023. Downloaded on 1/29/2026 5:10:34 AM.
This article is licensed under a Creative Commons Attribution-NonCommercial 3.0 Unported Licence.

# 5. Conclusions

We detailed the development and evolution of a stability chamber that uses color change as a proxy for degradation, to create a semi-automated system to test perovskite performance under heat, illumination, and humidity. The specific aim was to generate machine-interpretable data in a high-throughput and low-cost manner. To achieve the target, we established calibrated color change as a proxy for structural perovskite degradation in thin films. It correlates with changes in device performance arising from perovskite degradation. We also established it as a valid proxy for structural change in bulk perovskite samples, confirmed by powder XRD. The first generation stability chamber was conceived at MIT, and developed into an open source platform that underwent further evolution at Haverford, Stanford, and MIT. At Haverford, the chamber was modified to work with small quantities of bulk crystals. At Stanford, the chamber was adapted to test full solar devices in a glove box. At MIT, the chamber was adapted with expanded dew point and spectral control.

In our reflection on the open hardware-development process and laboratory adoption, we found that an open source hardware platform dramatically reduces upfront time to develop bespoke equipment. The process of inter-laboratory transfer, and open source dissemination is improved through dedicated individuals at both push and pull sites, thorough documentation, and open lines of communication. Not only does this increase the rate at which new labs can get open hardware running, but it facilitates the process of hardware evolution, increasing the capabilities of the platform.

# 6. Experimental

## 6a. X-ray diffraction measurements and aging tests for thin film perovskite samples

The perovskite film data used in this work for clustering analysis is originally published in ref. 43 with full descriptions of the sample preparation and measurement processes. A condensed description is provided here in parts that are relevant for the clustering analysis. The perovskite thin films analyzed in this work were spin-coated on cleaned and UV-ozone-treated glass substrates. Over-stoichiometric $PbI_2$ was used for synthesizing all the films in a molar ratio of 1.09 ($PbI_2$) to 1 (CsI, MAI, and FAI). Lead(II) iodide solution was prepared in 9 : 1 *N*,*N*-dimethylformamide to dimethyl sulfoxide solvent. The precursor solutions were mixed to their nominal Cs-FA-MA compositions, chlorobenzene antisolvent was used in the spin-coating, and the spin-coated films were annealed at 403 K for 20 min before cooling them down to room temperature, cutting them in halves, and transporting the other half to XRD measurements and the other half to the degradation test. Grazing incidence X-ray diffraction with incidence angle of 1° was performed with Rigaku Smartlab with Cu-Kalpha sources. Reference XRD spectra obtained from literature for delta-CsPbI3,[57] delta-FAPbI3,[58] and alpha-perovskite[43] were used as the basis of the XRD analyses. It should be noted that the thin film samples have lattice strain leading to peak shifts in the spectra compared to the reference powder samples. It should be also noted that some of the compositions were prepared multiple times and thus have duplicate XRD measurements. The degradation tests for the films were performed under 85 ± 2 °C sample holder temperature, 85 ± 5% air humidity, and 0.15 ± 0.01 Sun visible light only illumination for 7000 minutes using the first generation degradation chamber presented in this work. During this time, the samples were photographed automatically with 5 minutes intervals. The handling histories of the samples directed to XRD or degradation differ starting from the time point they were halved (for example, different times of storage before measurement). In total 168 films with varying compositions were prepared (some with duplicate compositions).

Camera data treatment for hierarchical clustering: one perovskite film was dropped from the analysis (flagged as poor quality already during sample preparation) and 5 reference samples with Br content (detected in by the clustering algorithm as their own cluster) were dropped from the analysis as the purpose was to focus on iodide-only samples. There were no missing or faulty time points in the camera data. The raw camera data was color calibrated *via* three-dimensional thin-plate spline method and sample colors extracted automatically with the default software of Generation 1 chamber as described in chamber implementations. The red, green, and blue channel time series of the color-calibrated RGB data were appended one after another for the clustering analysis.

XRD data treatment for hierarchical clustering: one XRD spectrum was dropped from the analysis since the sample composition could not be confirmed from the manually written file name. All the XRD data was resampled to the same angle resolution and normalized before clustering. XRD data with normalization and no resampling is shown in the figures in this work.

Hierarchical clustering: the color-calibrated film color as a function of aging test duration data were clustered using a hierarchical clustering algorithm.[59] Hierarchical clustering was chosen among the clustering algorithms due to the graphical analysis of the suggestive number of clusters, which is ideal for the future repeated use of the degradation data clustering repository in repeated retrospective analysis of the degradation test data, should the users prefer to choose the cluster centroid samples for spot-checks or in-depth characterization. Hierarchical cluster distances were determined using UPGMA algorithm and cosine distance measure that we deemed suitable for spectral and time series data was used. In the resulting dendrogram, three distinct clusters were detected for both XRD and RGB datasets. Silhouette index with the cosine metric (calculated in the XRD or RGB plane) and Davies–Bouldin index with the Euclidean metric (calculated in the composition plane) were used for selecting the correct number of clusters for the respective datasets. The hierarchical clustering was repeated multiple times with different numbers of clusters and the number with the highest average silhouette score and the lowest Davies–Bouldin index (both indicating the best cluster separation), and the highest silhouette values for individual samples, was chosen. A *k*-means clustering


© 2023 The Author(s). Published by the Royal Society of Chemistry

Open Access Article. Published on 13 February 2023. Downloaded on 1/29/2026 5:10:34 AM.
This article is licensed under a Creative Commons Attribution-NonCommercial 3.0 Unported Licence.

procedure was additionally utilized as a reference method to confirm that the cluster division is robust towards the clustering method of choice. As the *k*-means algorithm uses the Euclidean distance metric by definition, the *k*-means input data was transformed with the cosine kernel principal component analysis approach. Cluster centroids here were selected based on the smallest Euclidean distance to the cluster average XRD spectrum or degradation curve for the XRD and RGB data, respectively. Cluster centroids were exposed to a detailed analysis as the typical representatives of each cluster.

### 6b. X-ray diffraction measurements and aging tests for bulk crystal perovskite samples

The perovskite bulk sample data used in this work was created in a workflow modified to make ground samples for degradation analysis. The perovskite crystals were synthesized using bench scale antisolvent vapor diffusion. The two bulk crystal samples were prepared from stock solutions of methylammonium and lead(II) iodide dissolved in gamma-butyrolactone, and cyclohexylmethylammonium and lead(II) iodide dissolved in gamma-butyrolactone. The crystals were grown over the course of 48 hours, then filtered and dried. Powder X-ray diffraction measurements were performed on a Rigaku MiniFlex X-ray diffractometer using CuK$\alpha$ radiation (1.5418 Å). Rigaku Smartlab was used to confirm the correct sample identity, reference XRD spectra were obtained from literature for [CHMA][$PbI_4$],[60] and for $MAPbI_3$.[61] The remaining sample was preserved in a vacuum desiccator until aging chamber longitudinal testing. Longitudinal testing was started less than 48 hours after sample synthesis. Samples were manually ground by mortar and pestle to a fine powder. Powder X-ray diffraction measurements were taken one more time, to both ensure that degradation had not occurred, and to provide a pre-degradation powder pattern.

To prepare the bulk samples for degradation testing, the powder was spread finely across 10 mm filter paper to enable uniform degradation across the sample and increase kinetics. Each different compound was plated in duplicate to ensure enough yield for post-degradation powder X-ray diffraction, and to further confirm uniformity across different sample locations. No significant spatial differences were found in post-characterization. Once loaded in the chamber, samples were held at 0.15 ± 0.01 Sun, under 85 ± 2 °C sample tray temperature, and 85 ± 5% air humidity for ~150 hours. To minimize potential temperature differences, samples are constrained to a heated sample holder with high thermal conductivity. No significant temperature, or humidity variations across the sample holder were detectable *via* melt-temp standards and external humidity probes. To minimize variations of light intensity, samples were placed only within a small radius at the center of the lamp's illumination. Samples in the chamber were imaged every minute. Raw camera color data was color calibrated using the previously described method of the MIT Gen. 1 Chamber. After the degradation testing concluded, the samples were removed from the chamber and post-powder X-ray diffraction measurements were taken.

## Data and code availability

Fig. 3 and 4 as well as ESI Fig. S2–S4† in this article contain new, unpublished analyses. The data in Fig. 4 and ESI Fig. S4† are available on Figshare. The data in Fig. 3 and ESI Fig. S2, S3† have been made publicly available by the authors in an earlier work[43] and are now exposed to clustering analysis. The aging test images and metadata are available on Figshare due to their large file sizes:

- **https://figshare.com/articles/dataset/MA_CHMA_pXRD_Peaks_Pre_Post/20407794**
- **https://figshare.com/articles/dataset/MA_CHMA_System_Pre_Post_pXRD_xls/20407758**
- **https://figshare.com/articles/dataset/Haverford_Aging_Chamber_Output_For_MA_CHMA_Perovskite_System_Updated_/21944228**
- **https://doi.org/10.6084/m9.figshare.20506857**
- **https://doi.org/10.6084/m9.figshare.20523327**
- **https://doi.org/10.6084/m9.figshare.20521173**

The aging test image data rendered into a widely useable form (*i.e.*, csv files with raw and color-calibrated color as a function of time for each sample and metadata files with sample compositions) and XRD data, as well as the analysis codes directly reproducing Fig. 3 and ESI Fig. S2† are shared in an open repository:

- **https://github.com/PV-Lab/cluster-perovskite-data**

All the documentation, CAD drawings, control and analysis codes, and calibration data of the four degradation chambers presented in this work are shared in the following open repositories.

MIT Gen. 1 build and analysis of the image data (version used for this work is 1.0):

- **https://github.com/PV-Lab/hte_degradation_chamber**
- **https://github.com/PV-Lab/RGBanalysis**

Haverford Gen. 2 build and analysis of the image data (version used for this work is Haverford_1.0):

- **https://github.com/rodolfokeesey/Haverford_Environmental_Chamber**

Stanford Gen. 2 build and analysis of the image data (version used for this work is Stanford_1.0):

- **https://github.com/ThomasWColburn/Stanford-Environmental-Chamber**

MIT Gen. 2 build (control and analysis with MIT Gen. 1 codes):

- **https://github.com/PV-Lab/hte_degradation_chamber_gen2**

## Author contributions

Authors R. K., A. T., C. B., A. E., and S. T. wrote codes for the chamber use and data analysis; R. K., A. T., T. C., J. S., M. Z., K. H., C. G., A. E., and Z. L. built the equipment; R. K., A. T., A. S., T. C., S. S., N. H., Z. L., F. O., J. T., A. N., and T. B. conceived of and executed the experiments; and A. T., R. D., A. N., and T. B. conceptualized and supervised the research. Authors R. K., A. T., A. S., A. N., and T. B. wrote the first version of the manuscript. All the authors participated in planning of the work and reviewing and editing the manuscript.

© 2023 The Author(s). Published by the Royal Society of Chemistry

Open Access Article. Published on 13 February 2023. Downloaded on 1/29/2026 5:10:34 AM.
This article is licensed under a Creative Commons Attribution-NonCommercial 3.0 Unported Licence.

## Conflicts of interest

Two of the authors (ZL, TB) own equity in a startup company, Xinterra Pte. Ltd, which applies machine learning to accelerate materials development. One of the authors (AJN) is a scientific advisor to Atinary, which applies machine learning to accelerate materials development. We open sourced all information in this study to ensure that all benefit equally.

## Acknowledgements

The authors thank Antonio Buscemi and Isaac Metcalf for assistance in XRD measurements, and Shreyaa Raghavan for the development of the user-friendly Python package. This study is based upon work supported by the Defense Advanced Research Projects Agency (DARPA) under contract no. HR001118C0036. Any opinions, findings and conclusions or recommendations expressed in this material are those of the authors and do not necessarily reflect the views of DARPA. S. S., N. T. P. H., A. T., and T. B. thank TOTAL S. A. The research is also supported by Singapore Massachusetts Institute of Technology (MIT) Alliance for Research and Technology's Low Energy Electronic Systems research program. A. T. was supported by the Academy of Finland (Flagship program: Finnish Center for Artificial Intelligence FCAI). F. O. was supported by the U.S. Department of Energy under Photovoltaic Research and Development program under award DE-EE0007535. T. W. C. acknowledges the support from the Graduate Research Fellowship Program (award no. DGE-656518) from the U.S. National Science Foundation.

## References

1 Y. Fu, J. Li, H. Luo, C. Du and X. Li, Recent advances on environmental corrosion behavior and mechanism of high-entropy alloys, *J. Mater. Sci. Technol.*, 2021, **80**, 217–233, DOI: **10.1016/j.jmst.2020.11.044**.

2 N. Birbilis, S. Choudhary, J. R. Scully and M. L. Taheri, A perspective on corrosion of multi-principal element alloys, *npj Mater. Degrad.*, 2021, **5**(1), 1, DOI: **10.1038/s41529-021-00163-8**.

3 Y. Luo, K. Song, X. Ding and X. Wu, Environmental sustainability of textiles and apparel: a review of evaluation methods, *Environ. Impact Assess. Rev.*, 2021, **86**, 106497, DOI: **10.1016/j.eiar.2020.106497**.

4 J.-M. Kim, X. Zhang, J.-G. Zhang, A. Manthiram, Y. S. Meng and W. Xu, A review on the stability and surface modification of layered transition-metal oxide cathodes, *Mater. Today*, 2021, **46**, 155–182, DOI: **10.1016/j.mattod.2020.12.017**.

5 J. Yuan, *et al.*, Membranes in non-aqueous redox flow battery: a review, *J. Power Sources*, 2021, **500**, 229983, DOI: **10.1016/j.jpowsour.2021.229983**.

6 Thermo Scientific Forma Environmental Chamber Model 3911, 311.5 L, Stainless Steel - Incubators, Environmental Chambers, **https://www.fishersci.com/shop/products/forma-environmental-chamber-model-3911-311-5-l-stainless-steel/13987065**, accessed April 05, 2022.

7 M. M. Flores-Leonar, *et al.*, Materials acceleration platforms: on the way to autonomous experimentation, *Curr. Opin. Green Sustainable Chem.*, 2020, **25**, 100370, DOI: **10.1016/j.cogsc.2020.100370**.

8 E. Stach, *et al.*, Autonomous experimentation systems for materials development: a community perspective, *Matter*, 2021, **4**(9), 9.

9 J. Yano, *et al.*, The case for data science in experimental chemistry: examples and recommendations, *Nat. Rev. Chem.*, 2022, 1–14, DOI: **10.1038/s41570-022-00382-w**.

10 P. Goel, *et al.*, Perovskite materials as superior and powerful platforms for energy conversion and storage applications, *Nano Energy*, 2021, **80**, 105552, DOI: **10.1016/j.nanoen.2020.105552**.

11 H. Kim, J. S. Han, J. Choi, S. Y. Kim and H. W. Jang, Halide Perovskites for Applications beyond Photovoltaics, *Small Methods*, 2018, **2**(3), 1700310, DOI: **10.1002/smtd.201700310**.

12 S. Mazumdar, Y. Zhao and X. Zhang, Stability of Perovskite Solar Cells: Degradation Mechanisms and Remedies, *Front. Electron.*, 2021, **2**, 712785.

13 A. Urbina, The balance between efficiency, stability and environmental impacts in perovskite solar cells: a review, *J. Phys.: Energy*, 2020, **2**(2), 022001, DOI: **10.1088/2515-7655/ab5eee**.

14 T. J. Jacobsson, *et al.*, An open-access database and analysis tool for perovskite solar cells based on the FAIR data principles, *Nat. Energy*, 2022, **7**(1), 1, DOI: **10.1038/s41560-021-00941-3**.

15 M. V. Khenkin, *et al.*, Consensus statement for stability assessment and reporting for perovskite photovoltaics based on ISOS procedures, *Nat. Energy*, 2020, **5**(1), 1, DOI: **10.1038/s41560-019-0529-5**.

16 W. Fu, *et al.*, Stability of perovskite materials and devices, *Mater. Today*, 2022, **52**(1), DOI: **10.1016/j.mattod.2022.06.020**.

17 C. C. Boyd, R. Cheacharoen, T. Leijtens and M. D. McGehee, Understanding Degradation Mechanisms and Improving Stability of Perovskite Photovoltaics, *Chem. Rev.*, 2019, **119**(5), 3418–3451, DOI: **10.1021/acs.chemrev.8b00336**.

18 R. Azmi, *et al.*, Damp heat–stable perovskite solar cells with tailored-dimensionality 2D/3D heterojunctions, *Science*, 2022, **376**(6588), 73–77, DOI: **10.1126/science.abm5784**.

19 A. H. Slavney, R. W. Smaha, I. C. Smith, A. Jaffe, D. Umeyama and H. I. Karunadasa, Chemical Approaches to Addressing the Instability and Toxicity of Lead–Halide Perovskite Absorbers, *Inorg. Chem.*, 2017, **56**(1), 46–55, DOI: **10.1021/acs.inorgchem.6b01336**.

20 S. Cheng and H. Zhong, What Happens When Halide Perovskites Meet with Water?, *J. Phys. Chem. Lett.*, 2022, **13**(10), 2281–2290, DOI: **10.1021/acs.jpclett.2c00166**.

21 Opentrons | Open-source Lab Automation, Starting at $5,000, **https://opentrons.com/**, accessed November 30, 2021.

22 D. C. Florian, M. Odziomek, C. L. Ock, H. Chen and S. A. Guelcher, Principles of computer-controlled linear


© 2023 The Author(s). Published by the Royal Society of Chemistry

Open Access Article. Published on 13 February 2023. Downloaded on 1/29/2026 5:10:34 AM. This article is licensed under a Creative Commons Attribution-NonCommercial 3.0 Unported Licence.

motion applied to an open-source affordable liquid handler for automated micropipetting, *Sci. Rep.*, 2020, **10**(1), 13663, DOI: 10.1038/s41598-020-70465-5.

23 F. Barthels, U. Barthels, M. Schwickert and T. Schirmeister, FINDUS: An Open-Source 3D Printable Liquid-Handling Workstation for Laboratory Automation in Life Sciences, *SLAS Technology: Translating Life Sciences Innovation*, 2020, **25**(2), 190–199, DOI: 10.1177/2472630319877374.

24 M. C. Carvalho and R. H. Murray, Osmar, the open-source microsyringe autosampler, *HardwareX*, 2018, **3**, 10–38, DOI: 10.1016/j.ohx.2018.01.001.

25 R. Keesey, R. LeSuer and J. Schrier, Sidekick: a low-cost open-source 3D-printed liquid dispensing robot, *HardwareX*, 2022, **12**, DOI: 10.1016/j.ohx.2022.e00319.

26 M. Shahabi, S. Rafiee, S. S. Mohtasebi and S. Hosseinpour, Image analysis and green tea color change kinetics during thin-layer drying, *Food Sci. Technol. Int.*, 2014, **20**(6), 465–476, DOI: 10.1177/1082013213492524.

27 A. Antonelli, *et al.*, Automated evaluation of food colour by means of multivariate image analysis coupled to a wavelet-based classification algorithm, *Anal. Chim. Acta*, 2004, **515**(1), 3–13, DOI: 10.1016/j.aca.2004.01.005.

28 E. M. Gonçalves, J. Pinheiro, M. Abreu, T. R. S. Brandão and C. L. M. Silva, Modelling the kinetics of peroxidase inactivation, colour and texture changes of pumpkin (Cucurbita maxima L.) during blanching, *J. Food Eng.*, 2007, **81**(4), 693–701, DOI: 10.1016/j.jfoodeng.2007.01.011.

29 H. Landolt, Ueber die Zeitdauer der Reaction zwischen Jodsäure und schwefliger Säure, *Ber. Dtsch. Chem. Ges.*, 1886, **19**(1), 1317–1365, DOI: 10.1002/cber.188601901293.

30 L. Madriz, F. M. Cabrerizo and R. Vargas, Exploring Chemical Kinetics at Home in Times of Pandemic: Following the Bleaching of Food Dye Allura Red Using a Smartphone, *J. Chem. Educ.*, 2021, **98**(6), 2117–2121, DOI: 10.1021/acs.jchemed.0c01427.

31 R. W. G. Hunt and M. R. Pointer, *Measuring Colour*, John Wiley & Sons, 2011.

32 G. D. Finlayson, M. Mackiewicz and A. Hurlbert, Color Correction Using Root-Polynomial Regression, *IEEE Trans. Image Process.*, 2015, **24**(5), 1460–1470, DOI: 10.1109/TIP.2015.2405336.

33 P. Menesatti, C. Angelini, F. Pallottino, F. Antonucci, J. Aguzzi and C. Costa, RGB Color Calibration for Quantitative Image Analysis: The '3D Thin-Plate Spline' Warping Approach, *Sensors*, 2012, **12**(6), 6, DOI: 10.3390/s120607063.

34 M. I. Asghar, K. Miettunen, S. Mastroianni, J. Halme, H. Vahlman and P. Lund, *In situ* image processing method to investigate performance and stability of dye solar cells, *Sol. Energy*, 2012, **86**(1), 331–338, DOI: 10.1016/j.solener.2011.10.006.

35 R. R. Naik, *et al.*, Discovering equations that govern experimental materials stability under environmental stress using scientific machine learning, *npj Comput. Mater.*, 2022, **8**(1), 1, DOI: 10.1038/s41524-022-00751-5.

36 D. Wu and D.-W. Sun, Colour measurements by computer vision for food quality control – a review, *Trends Food Sci. Technol.*, 2013, **29**(1), 5–20, DOI: 10.1016/j.tifs.2012.08.004.

37 C. Yan, *et al.*, Computer Vision for Understanding Catalyst Degradation Kinetics, *ChemRxiv*, 2022, DOI: 10.26434/chemrxiv-2022-n0wf3.

38 C. Zeng, *et al.*, A platinum modulated tungsten oxide on Ag nanowires network as an indicator for in-situ visualized evaluation of the hydrogen evolution performance, *Int. J. Hydrogen Energy*, 2023, **48**(9), 3364–3372, DOI: 10.1016/j.ijhydene.2022.10.217.

39 Y. Zhang, Z. Chen and Z. Lu, A Facile Method for the Preparation of Colored $Bi_4Ti_3O_{12-x}$ Nanosheets with Enhanced Visible-Light Photocatalytic Hydrogen Evolution Activity, *Nanomaterials*, 2018, **8**(4), 4, DOI: 10.3390/nano8040261.

40 S. G. Hashmi, *et al.*, Long term stability of air processed inkjet infiltrated carbon-based printed perovskite solar cells under intense ultra-violet light soaking, *J. Mater. Chem. A*, 2017, **5**(10), 4797–4802, DOI: 10.1039/C6TA10605F.

41 X. H. Zhu, Z. R. Wei, Y. R. Jin and A. P. Xiang, Growth and characterization of a $PbI_2$ single crystal used for gamma ray detectors, *Cryst. Res. Technol.*, 2007, **42**(5), 456–459, DOI: 10.1002/crat.200610847.

42 M. K. A. Mohammed, A. Al-Mousoi, M. Mehde and A. Al-Gebori, Engineered electronic properties of the spin-coated MAPI for hole-transport-free perovskite solar cell (HT-free PSC): spinning time and PSC performance relationship, *Chem. Phys. Lett.*, 2020, **754**, 137718, DOI: 10.1016/j.cplett.2020.137718.

43 S. Sun, *et al.*, A data fusion approach to optimize compositional stability of halide perovskites, *Matter*, 2021, **4**(4), 1305–1322, DOI: 10.1016/j.matt.2021.01.008.

44 Z. Kolláth, A. Cool, A. Jechow, K. Kolláth, D. Száz and K. P. Tong, Introducing the dark sky unit for multi-spectral measurement of the night sky quality with commercial digital cameras, *J. Quant. Spectrosc. Radiat. Transfer*, 2020, **253**, 107162, DOI: 10.1016/j.jqsrt.2020.107162.

45 Camera Basics, https://www.thorlabs.com/newgrouppage9.cfm?objectgroup_id=8962, accessed July 30, 2022.

46 R. J. Sutton, *et al.*, Cubic or Orthorhombic? Revealing the Crystal Structure of Metastable Black-Phase $CsPbI_3$ by Theory and Experiment, *ACS Energy Lett.*, 2018, **3**(8), 1787–1794, DOI: 10.1021/acsenergylett.8b00672.

47 N. Rolston, *et al.*, Rapid Open-Air Fabrication of Perovskite Solar Modules, *Joule*, 2020, **4**(12), 2675–2692, DOI: 10.1016/j.joule.2020.11.001.

48 S. Oberloier and J. M. Pearce, General Design Procedure for Free and Open-Source Hardware for Scientific Equipment, *Designs*, 2018, **2**(1), 1, DOI: 10.3390/designs2010002.

49 T. Baden, A. M. Chagas, G. Gage, T. Marzullo, L. L. Prieto-Godino and T. Euler, Open Labware: 3-D Printing Your Own Lab Equipment, *PLoS Biol.*, 2015, **13**(3), e1002086, DOI: 10.1371/journal.pbio.1002086.

© 2023 The Author(s). Published by the Royal Society of Chemistry

Open Access Article. Published on 13 February 2023. Downloaded on 1/29/2026 5:10:34 AM.
This article is licensed under a Creative Commons Attribution-NonCommercial 3.0 Unported Licence.

50 Stack Overflow - Where Developers Learn, Share, & Build Careers, Stack Overflow, **https://stackoverflow.com**, accessed April 15, 2022.
51 Thingiverse.com, Thingiverse - Digital Designs for Physical Objects, **https://www.thingiverse.com/**, accessed April 15, 2022.
52 GrabCAD Makes Additive Manufacturing at Scale Possible, **https://grabcad.com/**, accessed April 15, 2022.
53 J. M. Pearce, Economic savings for scientific free and open source technology: a review, *HardwareX*, 2020, **8**, e00139, DOI: **10.1016/j.ohx.2020.e00139**.
54 Build software better, together, GitHub, **https://github.com**, accessed April 15, 2022.
55 Adafruit Industries, Unique & fun DIY electronics and kits, **https://www.adafruit.com/?gclid=Cj0KCQjwr-SSBhC9ARIsANhzu15FYJS0vuUwgW6SCktyHpuvZCvQyBDO4HwqEnpSdShIP5UMHNKhOPYaAuq1EALw_wcB**, accessed April 15, 2022.
56 SparkFun Electronics, **https://www.sparkfun.com/?gclid=Cj0KCQjwr-SSBhC9ARIsANhzu16y1q_VGacLrdL3DJH6vk5USCryZC46oXuq_FhgPYaDQoM8wYeQj9EaArSIEALw_wcB**, accessed April 15, 2022.
57 D. B. Straus, S. Guo, A. M. Abeykoon and R. J. Cava, Understanding the Instability of the Halide Perovskite $CsPbI_3$ through Temperature-Dependent Structural Analysis, *Adv. Mater.*, 2020, **32**(32), 2001069, DOI: **10.1002/adma.202001069**.
58 O. J. Weber, *et al.*, Phase Behavior and Polymorphism of Formamidinium Lead Iodide, *Chem. Mater.*, 2018, **30**(11), 3768–3778, DOI: **10.1021/acs.chemmater.8b00862**.
59 D. Müllner, Modern hierarchical, agglomerative clustering algorithms, *arXiv*, 2011, DOI: **10.48550/arXiv.1109.2378**.
60 Z. Li, *et al.*, Robot-Accelerated Perovskite Investigation and Discovery, *Chem. Mater.*, 2020, **32**(13), 5650–5663, DOI: **10.1021/acs.chemmater.0c01153**.
61 J. Xie, *et al.*, Study on the correlations between the structure and photoelectric properties of $CH_3NH_3PbI_3$ perovskite light-harvesting material, *J. Power Sources*, 2015, **285**, 349–353, DOI: **10.1016/j.jpowsour.2015.03.114**.
62 F. Elsehrrawy, B. Blomsedt, E. Ilén, E Palovuori and J. Halme, Optimisation of knitted fabrics as visually concealing covers for textile-integrated photovoltaics, *Sol. Energy Mater. Sol. Cells*, 2023, **252**, 112205, DOI: **10.1016/j.solmat.2023.112205**.


© 2023 The Author(s). Published by the Royal Society of Chemistry